nature biotechnology

Article

https://doi.org/10.1038/s41587-026-03115-2

Immune-remodeling mRNAs expressing IRF8 or NIK generate durable antitumor immunity in multiple cancer models

Received: 23 September 2025

Accepted: 31 March 2026

Published online: 13 May 2026

Check for updates

A. Gupta[1,2,9], R. Das[3,9], K. Reed[1,2,9], T. Jeon[1,2], Q. T. C. Nguyen[1,2], A. Rudra[1,2,4], X. Ge[3], S. Trongjit[1,2], Y. S. Vanrobaeys[5], R. Langer[1,2], R. Weissleder[3,6,7], C. Garris[3,8] ✉ & D. G. Anderson[1,2] ✉

Although immunotherapy has benefited a subset of persons with cancer, its broader efficacy remains limited, primarily because of an immunosuppressive tumor microenvironment characterized by insufficient numbers of functional tumor-specific T cells, antigen-presenting cells (APCs) and tumor-infiltrating lymphocytes. Here we engineer immune cells in the tumor microenvironment using lipid nanoparticles (LNPs) to deliver immune-remodeling mRNAs (IR-mRNAs) encoding NF-κB-inducing kinase or interferon regulatory factor 8. These IR-mRNAs activate APCs in tumors, significantly increasing activated type 1 conventional dendritic cells, immunostimulatory cytokines and priming antitumor $CD8^+$ T cells. IR-mRNAs encapsulated in LNPs elicited durable antitumor responses in multiple syngeneic mouse tumor models through both intratumoral and intravenous delivery. Coadministration of IR-mRNA and ovalbumin mRNA elicited a ~10-fold increase in antigen-specific $CD8^+$ T cell responses, sustained long-term memory and effectively prevented tumor growth in vaccinated mice. Additionally, coadministration of IR-mRNA and hemagglutinin mRNA enhanced the humoral response ~5-fold and the cellular response ~15-fold, underscoring their potential as adjuvants for boosting adaptive immunity.

Cancer can develop numerous mechanisms of immune evasion, including immune cell exclusion, downregulation of tumor antigen presentation and promotion of immunosuppressive immune cell phenotypes[1–3]. Immunotherapies aim to overcome this immune evasion by triggering immunostimulation or by reprogramming the immune system to generate antitumor immunity. These treatment paradigms have improved outcomes in many cancers and there are now more than 60 immunotherapies approved by the US Food and Drug Administration[4]. Unfortunately, many individuals remain unresponsive to existing therapies[5,6]. There remains a need, therefore, for continued development of immunotherapies to overcome this resistance to treatment and improve treatment responses.

mRNA lipid nanoparticle (LNP)-based therapeutics have emerged as a potent modality for the transient expression of proteins for a range of disease applications[7]. These systems have the potential to address the unmet needs of existing immunotherapies by enabling transient

[1]David H. Koch Institute for Integrative Cancer Research, Massachusetts Institute of Technology, Cambridge, MA, USA. [2]Department of Chemical Engineering, Massachusetts Institute of Technology, Cambridge, MA, USA. [3]Center for Systems Biology, Massachusetts General Hospital, Boston, MA, USA. [4]Department of Anesthesiology, Critical Care and Pain Medicine, Boston Children's Hospital, Boston, MA, USA. [5]Bioinformatics & Computing Core Facility of the Swanson Biotechnology Center, Koch Institute for Integrative Cancer Research, Massachusetts Institute of Technology, Cambridge, MA, USA. [6]Department of Systems Biology, Harvard Medical School, Boston, MA, USA. [7]Department of Radiology, Massachusetts General Brigham, Boston, MA, USA. [8]Department of Pathology, Massachusetts General Hospital, Boston, MA, USA. [9]These authors contributed equally: A. Gupta, R. Das, K. Reed. ✉e-mail: cgarris@mgh.harvard.edu; dgander@mit.edu

expression of cytokines[8]. Transient delivery of mRNA-encoded effector molecules can augment adaptive immunity while mitigating toxicities from sustained exposure[9,10]. For example, RNA encoding proinflammatory cytokines delivered either intratumorally (IT; interleukin (IL)-23, IL-36γ and OX40L cocktail) or systemically (IL-12) have been used to generate antitumor responses[11,12]. Similarly, codelivery of IL-12 mRNA has shown to boost the immune response to SARS-CoV-2 vaccines in preclinical studies[13]. Despite this progress, effector-centric strategies have limitations; cytokine signals are often self-limiting when devoid of the context of additional signaling molecules[14,15]. Secreted cytokines may also diffuse away from immune cells, thereby preventing appropriate local immune activation while simultaneously causing systemic adverse events[16–18]. While these previous studies used secreted or transmembrane immune effectors, mRNA-LNPs also enable cytosolic expression of lineage-defining transcription factors and signaling kinases that control cell fate and activation states of immune cells. In contrast to cytokines and surface receptors, these intracellular factors can be used to simultaneously activate a diverse set of signaling cascades and reprogram immune cell phenotypes.

Given the potential advantages of intracellular factors, we sought to identify factors that could be used to engineer myeloid cell subsets such as macrophages and dendritic cells (DCs), which orchestrate tumor antigen presentation and priming of cytotoxic T cells[2,19]. We identified two factors that could affect myeloid cell maturation, the NF-κB-inducing kinase (NIK) and interferon (IFN) regulatory factor 8 (IRF8). NIK, a pivotal activator of the noncanonical NF-κB pathway that lies downstream of CD40 signaling, enhances DC–T cell crosstalk and augments responses to checkpoint blockade[20–22]. IRF8 is a lineage-defining factor required for type 1 conventional DC (cDC1) development and antigen cross-presentation[23–25]. Both act upstream of multiple effector signals and can drive proinflammatory cytokine production and myeloid polarization toward antitumor states[26,27]. Exploiting NIK therapeutically, however, has proven difficult. Approaches that rely on cellular inhibitor of apoptosis proteins (cIAPs) inhibition to stabilize NIK and trigger noncanonical NF-κB signaling are limited by efficacy and toxicity and there are no clinically deployed NIK agonists[28,29]. Previous efforts to harness IRF8 have been more successful; viral delivery of IRF8 with other transcription factors (PU.1/BATF3) has been shown to reprogram various cells into cDC1-like phenotypes, resulting in improved T cell priming and tumor regression in vivo[30,31]. However, this strategy has only been demonstrated for ex vivo engineering or IT administration, which is limited by the complexity of ex vivo DC vaccines and the invasive nature of IT administration[32,33]. Moreover, the use of viral vectors in vivo may present challenges because of antivector immune responses and the resultant long-term expression of immunostimulatory genes[34,35]. We hypothesized that mRNA-LNP delivery of NIK or IRF8, which we term immune-remodeling mRNAs (IR-mRNAs), could overcome these limitations and enable productive myeloid cell maturation and immune responses.

Therefore, we formulated either NIK or IRF8 mRNA into LNPs and found that they induced strong antitumor efficacy across multiple syngeneic models through intravenous (IV) or IT dosing and generated durable immune memory, evidenced by complete protection upon rechallenge. Additionally, to assess cancer vaccine potential, these IR-mRNAs were codelivered with ovalbumin (OVA) mRNA (a model antigen), which significantly increased circulating OVA-specific $CD8^+$ T cells to approximately 25%. This response was also durable, persisting at least 90 days, and effectively prevented B16-OVA tumor growth in vaccinated mice. Furthermore, these IR-mRNAs markedly boosted adaptive immune responses when used with hemagglutinin (influenza A H3N2) and spike (SARS-CoV-2) antigens, highlighting their broad applicability for both cancer and infectious disease therapeutics. Mechanistic investigations revealed that these immune stimulants work by (1) activating antigen-presenting cells (APCs) and inducing DC maturation into a cDC1 phenotype; (2) inducing expression of proinflammatory signals to recruit additional immune cells to the tumor microenvironment; and (3) enhancing priming and activation of $CD8^+$ T cells.

Overall, this approach contrasts with mRNA therapeutics that rely on delivering isolated effector molecules such as cytokines or costimulatory receptors. NIK and IRF8 instead serve as pleiotropic immune activators, engaging multiple distinct immune pathways through a single mRNA payload. This advancement in mRNA target design lays the foundation for next-generation therapies, potentially enabling diverse applications to enhance immune responses in contexts such as cancer immunotherapy and vaccination, with broad translational potential.

In vitro efficacy of NIK and IRF8 mRNA in primary myeloid cells leading to activation of innate immunity pathways and cell phenotype differentiation

NIK and IRF8 act upstream of multiple effector pathways and are associated with increased proinflammatory cytokine production[22,25]. Therefore, to initially evaluate the immunostimulatory potential of IR-mRNAs, we formulated them with MessengerMAX (MMax) and administered them to immature bone-marrow-derived DCs (BMDCs) (Fig. 1a). We then examined activation of various immune signaling pathways. To evaluate IL-12 induction, we used BMDCs from p40-IRES-eYFP reporter mice, which express eYFP under the control of the IL-12p40 promoter. IL-12p40 reporters are widely used as validated surrogates for IL-12p70 secretion because of the well-established correlation between IL-12p40 expression and IL-12p70 production[36–38]. We observed significantly higher eYFP levels in both IR-mRNA-treated cells relative to the control firefly luciferase (FLuc) mRNA treatment, indicating sequence-specific upregulation of IL-12p40 (Fig. 1b,c and Supplementary Fig. 1a). IL-12 is involved in Th1 cell differentiation and maturing cytotoxic T cell antitumor immunity[39]; therefore, we believe that this enhanced expression of IL-12p40 may indicate that these IR-mRNAs strengthen the ability of DCs to activate cell-mediated

Fig. 1 | IR-mRNA induce BMDC maturation. a, Strategy for evaluating immune maturation in BMDCs. **b**, Fluorescence microscopy images showing IL-12p40–eYFP reporter expression levels in treated BMDCs from IL-12p40–eYFP reporter mice. Scale bar, 50 µm. **c**, Image analysis quantifying IL-12p40–eYFP reporter expression following treatment of BMDCs with 20 ng of mRNA. Data shown are the mean ± s.d. ($n = 3$ wells, pooled from five mice). **d**, Expression of IFNα and IFNβ in the cell culture supernatant following treatment of wild-type BMDCs with 20 ng of mRNA. Data shown are the mean ± s.d. ($n = 3$ wells, pooled from five mice). **e**, Flow cytometry quantification of maturation markers in BMDCs from C57Bl/6J mice following treatment with 50 ng of mRNA on days 0, 5 and 9. Data shown are the mean ± s.d. ($n = 3$ wells, pooled from five mice). **f**,**g**, Flow cytometry plots showing cDC1 phenotyping of BMDCs following mRNA treatment (**f**) and percentage cDC1 cells after IR-mRNA treatment (**g**). Data shown are the mean ($n = 6$ wells, pooled from ten mice). **h**, Uniform manifold approximation and projection plots showing scRNA-seq data from BMDCs isolated from C57Bl/6J mice following IRF8 treatment. **i**, Feature plots of IL-12p40 expression across cell clusters identified in **h**. Data shown are the mean ± s.d. ($n = 3$ wells). **j**–**i**, Monocole pseudotime reconstruction of DC progenitor, pDC, cDC1 and cDC2 populations following treatment of BMDCs with mRNA. Psuedotime analysis showing the developmental branches of each cell type in mRNA-treated BMDCs (**j**), pseudotime trajectory analysis (**k**) and mRNA treatments overlaid on the pseudotime trajectory analysis (**l**). Statistical significance was analyzed using a one-way analysis of variance with a two-tailed Tukey's multiple-comparison test using a single pooled variance (**c**–**e**) or a Brown–Forsythe and Welch analysis of variance with a two-tailed Dunnet T3 multiple-comparison test (**g**). Data are representative of three independent experiments (**b**–**g**) or two independent experiments (**h**–**l**). Panel **a** created in BioRender; Gupta, A. https://biorender.com/itm02de (2026); Reed, K. https://biorender.com/1x18dh3 (2026).

https://doi.org/10.1038/s41587-026-03115-2

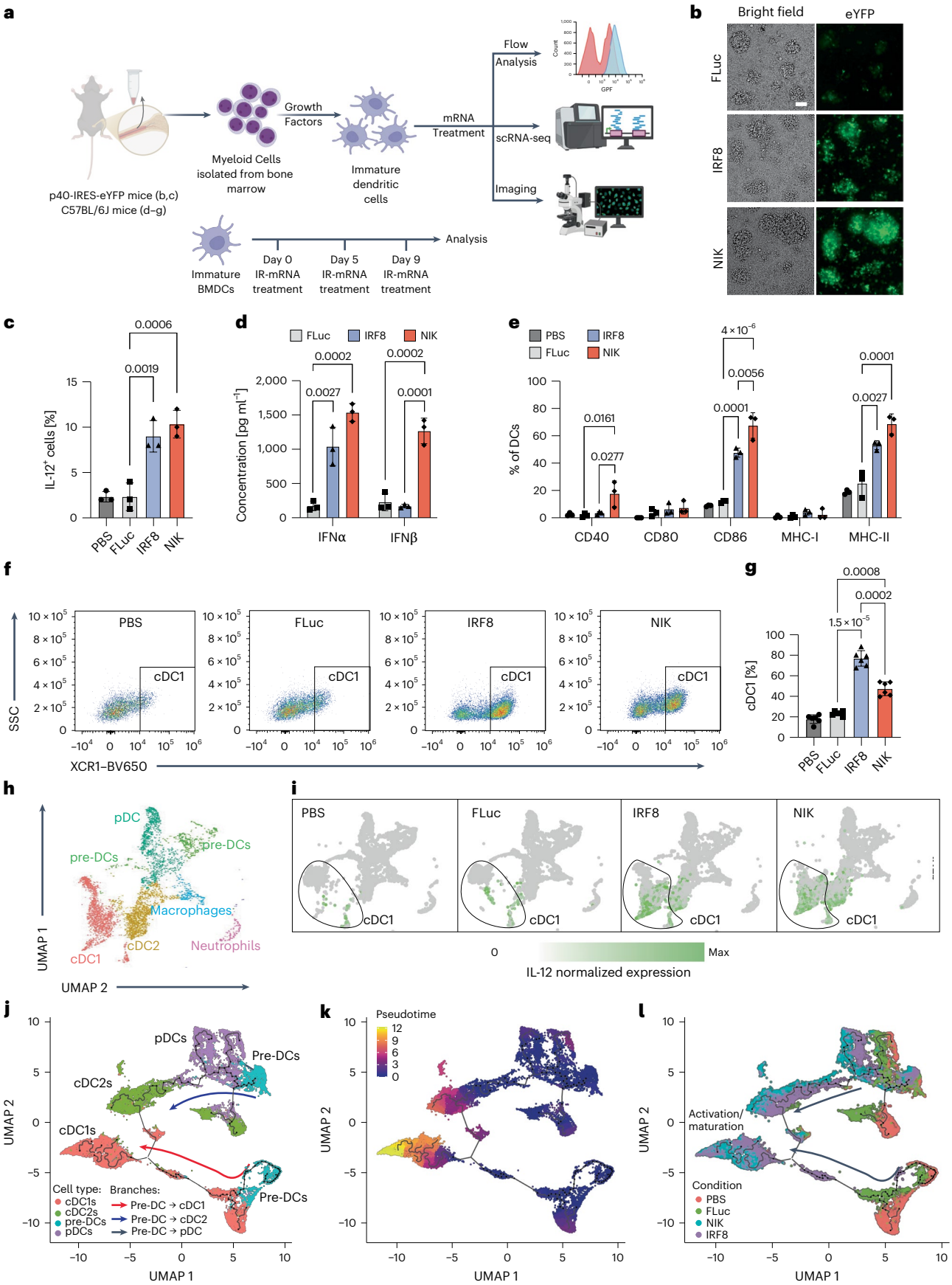

immunity[21]. We also assessed stimulation of IFN-I production following treatment with NIK and IRF8, as IFN-I is another important signal for T cell priming[40]. Transfection of wild-type C57BL/6J BMDCs with IR-mRNAs resulted in significantly higher IFN-I secretion compared to FLuc mRNA, further confirming their immunostimulatory potential. Notably, NIK induced the release of both IFNα and IFNβ, whereas IRF8 primarily stimulated IFNα production (Fig. 1d and Supplementary Fig. 1b,c). Notably, NIK elicited a stronger IFN response than IRF8, consistent with previous reports identifying NIK as a central signaling node in the noncanonical NF-κB pathway[20]. Overall, these results demonstrate the ability of these IR-mRNAs to induce the expression of key T cell priming signals.

We next investigated how IR-mRNAs modulate immature DCs to acquire mature phenotypes capable of efficient T cell priming, using flow cytometry and single-cell RNA sequencing (scRNA-seq). IR-mRNAs were again formulated with MMax and administered to immature BMDCs from wild-type C57BL/6J mice. Flow cytometry revealed a significant increase in the proportion of activated DCs, as evidenced by significant increases in CD86 and MHC-II (Fig. 1e and Supplementary Fig. 2). Furthermore, the proportion of cDC1 cells significantly increased following IR-mRNA treatment (Fig. 1f,g and Supplementary Fig. 3). Notably, IRF8 transfection resulted in ~77% of the total population adopting a cDC1 phenotype, representing a 4.3-fold increase compared to PBS and a ~3.3-fold increase compared to FLuc controls, consistent with IRF8's role in driving cDC1 lineage commitment[41]. NIK mRNA treatment also enhanced cDC1 differentiation, possibly because of the increased production of IFN-I and IL-12, both of which are known to support cDC1 development[23,42,43]. Consistent with flow cytometry results, the scRNA-seq results demonstrated an expansion of cDC1-like cells marked by *Batf3* expression (Supplementary Fig. 4)[24,44]. We also observed an increase in the cDC2 populations within IR-mRNA-treated BMDCs in scRNA-seq.

Within the BMDCs, we also observed a shift in phenotype in IR-mRNA-treated BMDCs, characterized by significant increases in *Il12b*, *Cd40*, *Cd80*, *Cd83*, *Cd86* and *Ccr7* expression (Fig. 1h,i and Supplementary Fig. 5). Notably, an increase in *Cd40/Cd80* transcription levels was not reflected in flow cytometry studies (Fig. 1e), suggesting that transcriptional activation does not always translate directly into surface protein accumulation[45]. Pre-DCs following IR-mRNA treatment revealed upregulation of transcription factors associated with cDC1 development, such as *Spi1* and *Irf8* (refs. 46,47). Concurrently, genes involved with antigen processing and cross-presentation, including *Ctsc*, *Nlrc5* and *Psmb9*, were also elevated[48]. Upregulation of *Ifit3*, *Irf7*, *Stat2* and *Stat3* indicated activation of IFN-I signaling[49] following IR-mRNA treatment (Supplementary Fig. 5).

Next, we performed a Monocle psuedotime analysis on the scRNA-seq data to determine whether cell remodeling was occurring through maturation pathways or cell fate conversion[50]. With DC progenitors selected as the trajectory root, the resulting principal graph identified two primary lineages: one leading to the cDC1 subset and another toward pDC and cDC2 populations (Fig. 1j). This suggests that IR-mRNA treatment primarily induces DC activation and maturation within the endogenous pre-DC to cDC maturation pathway, rather than inducing fate conversion from cDC2s or pDCs into cDC1s or altering overall lineage identity. Additionally, while both cDC1 and cDC2 clusters showed a significant increase in pseudotime relative to progenitors, the cDC1 population reached higher terminal pseudotime values (Fig. 1k) and these populations arose as the result of IR-mRNA treatment (Fig. 1l). This indicates a more extensive transcriptional remodeling of the cDC1 lineage in response to treatment, consistent with the expected biological activity of the IR-mRNAs in driving cDC1 development[51]. Collectively, these findings highlight the developmental, antigen-processing and immunostimulatory axes that define cDC1 function[46]. cDC1s are critical for the cross-priming of $CD8^+$ T cells and have a central role in cancer vaccine efficacy and T cell-mediated immunity, suggesting that these IR-mRNAs are capable of promoting an antitumor phenotype within BMDCs[44,52].

Lastly, we examined whether the APC maturation and differentiation effects observed in mice extend to human DCs. To this end, we synthesized human NIK and IRF8 mRNAs and evaluated their activity in human DCs differentiated from primary human bone-marrow-derived $CD34^+$ progenitors. Immature human DCs were treated with human NIK, IRF8 or FLuc control mRNAs and DC activation was assessed by measuring the expression of canonical maturation markers CD40, CD80 and CD86. Consistent with our murine BMDC findings, treatment with human IR-mRNAs resulted in significantly increased expression of DC activation markers compared to FLuc-treated controls (Extended Data Fig. 1a). Moreover, treatment of immature human DCs to IRF8 or NIK mRNAs promoted differentiation toward a cDC1-biased phenotype, with IRF8 producing the strongest effect, followed by NIK, while FLuc treatment did not alter differentiation relative to untreated cells (Extended Data Fig. 1b). Together, these results suggest that the IR-mRNA-based immunomodulatory approach is compatible with human DC biology and supports its potential for translational application.

In vivo assessment of immune remodeling and toxicity upon systemic administration of mRNA adjuvants

After confirming that these IR-mRNAs can activate APCs in vitro, we tested their ability to stimulate IFN-I expression and APC activation in vivo. To do so, we formulated NIK, IRF8 and FLuc mRNAs individually into LNPs using a previously reported formulation containing the ionizable lipid cKK-E12, 1,2-dioleoyl-*sn*-glycero-3-phosphoethanolamine (DOPE), cholesterol and 1,2-dimyristoyl-*rac*-glycero-3-methoxypolyethylene glycol-2000 (DMG-PEG2k), as this formulation was previously shown to give high levels of mRNA expression in the liver and APCs[53,54]. We then administered mRNA-LNPs IV and assessed their immunostimulatory effects (Fig. 2a). At 6 h after LNP administration, IFN-I levels were significantly higher in IR-mRNA-treated mice relative to both control mRNA and PBS-treated mice (Fig. 2b). Given that IFN-I induction enhances DC expression of major histocompatibility complex class II (MHC-II) and costimulatory molecules[55], we next evaluated the ability of the IR-mRNAs to upregulate APC activation markers in lymphoid tissues following systemic administration of LNPs. Treated mice exhibited elevated expression of costimulatory marker CD86 on cDCs isolated from the spleen and lymph nodes (Fig. 2c,d and Supplementary Figs. 6 and 7). In the spleen, CD86 was upregulated in approximately 30% of APCs in NIK-treated and IRF8-treated mice, compared to only ~2% in FLuc (control) mRNA-treated mice. Additionally, both NIK-treated and IRF8-treated mice demonstrated a marked increase in M1-polarized macrophages (~30–35% in the spleen and ~10% in the lymph nodes), relative to FLuc-treated controls (~2.5% in both tissues) (Fig. 2e,f), although this increase was not statistically significant in the lymph node for IRF8-treated mice. In agreement with our in vitro observations, these studies demonstrate that IR-mRNA-LNPs function to modulate key APCs toward a proinflammatory, mature phenotype, which is critical for potentiating antitumor immune responses[51,56].

Although these IR-mRNA-LNPs induce immune activation, systemic delivery of cytokines and mRNA-LNP therapies may be associated with acute immune and hepatic toxicities. Therefore, we also conducted a thorough toxicological evaluation to identify any potential IR-mRNA-specific toxicity. Mice were IV administered 1.5 mg kg^{-1} of mRNA (FLuc, NIK or IRF8) formulated into cKK-E12 LNPs and monitored for 6 days for changes in body weight, biochemical markers and histopathology (Extended Data Fig. 2a). We observed systemic upregulation of proinflammatory cytokines in mice treated with NIK (granulocyte-macrophage colony-stimulating factor (GM-CSF), IL-6, tumor necrosis factor (TNF), IFNα and IFNβ) and IRF8 (IFNα and IFNβ) at 6 h (Fig. 2b) but these returned to baseline levels by day 6

https://doi.org/10.1038/s41587-026-03115-2

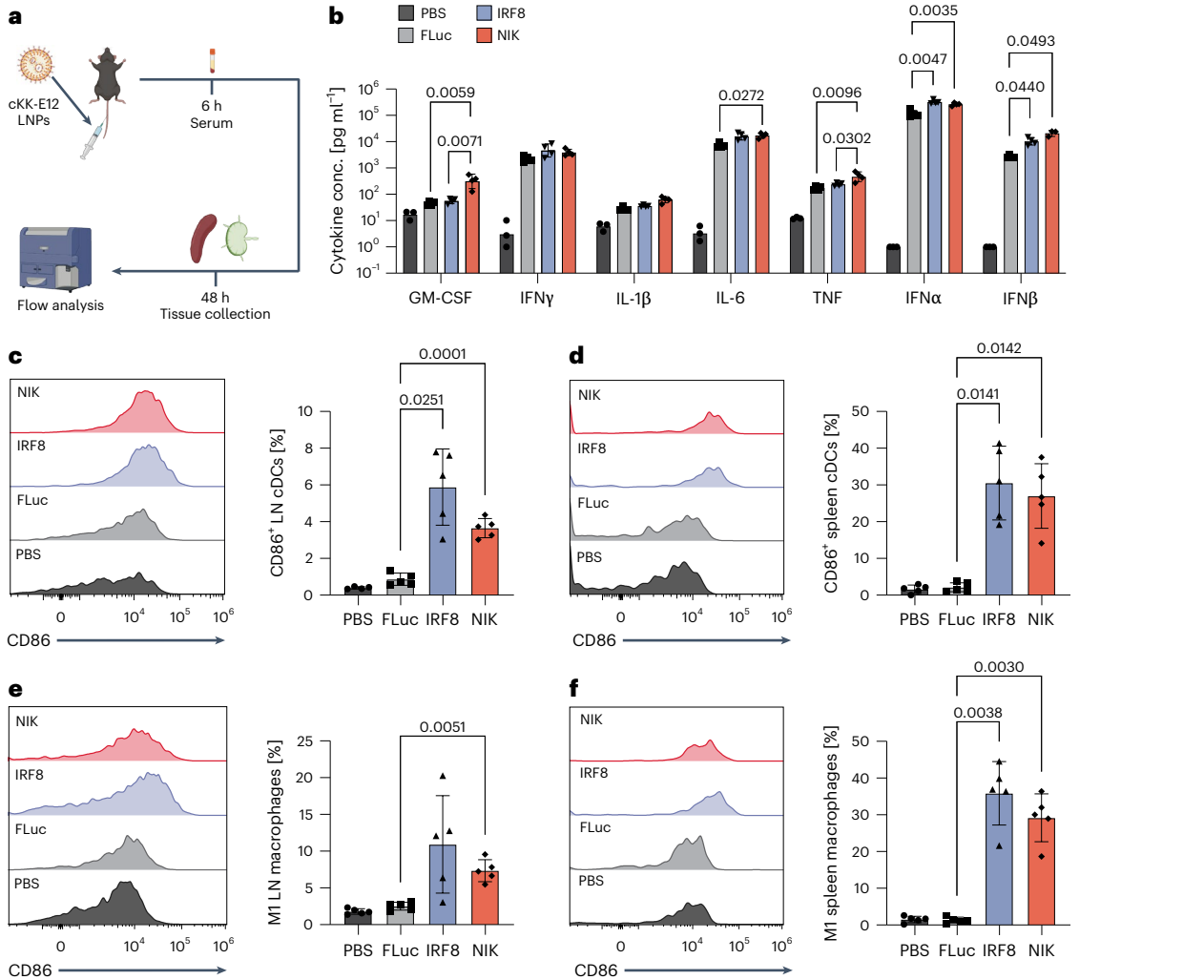

Fig. 2 | IR-mRNA active APCs in vivo. a, Strategy for evaluating APC activation. **b**, Serum cytokine concentrations 6 h after administration of mRNA-LNPs. Data shown are the mean ± s.d. ($n = 4$ mice). **c**,**d**, CD86 quantification in lymph node (**c**) and splenic (**d**) DCs 48 h after administration of mRNA-LNPs. Data shown are the mean ± s.d. ($n = 5$ mice). **e**,**f**, CD86 quantification in lymph node (**e**) and splenic (**f**) macrophages 48 h after administration of mRNA-LNPs. Data shown are the mean ± s.d. ($n = 5$ mice). Statistical significance was analyzed using a Brown–Forsythe and Welch analysis of variance with a two-tailed Dunnet T3 multiple-comparison test. Data are representative of two independent experiments (**c**–**f**) or one independent experiment (**b**). Panel **a** created in BioRender; Reed, K. https://biorender.com/kxqwfbg (2026).

(Extended Data Fig. 2b). Additionally, all mRNA-LNP-treated mice exhibited a similar, transient decrease in body weight at 6 h, which normalized to PBS-treated levels by day 4 (Extended Data Fig. 2c). Similarly, moderate hepatotoxicity, indicated by elevated serum aspartate aminotransferase (AST) and alanine aminotransferase (ALT) levels and reduced serum albumin at 6 h, was observed across all treatment groups, including FLuc controls. These changes largely resolve by day 6, with modest residual reductions in serum albumin for mRNA-LNP-treated groups (Extended Data Fig. 2d–h)[57]. Histopathological evaluation of the liver and spleen showed no significant differences between both IR-mRNAs and the control mRNA-treated mice (Supplementary Figs. 8 and 9). Overall, these results demonstrate that LNP-mediated delivery of NIK and IRF8 mRNA causes only transient and minimal systemic and hepatic inflammation, comparable to the FLuc control mRNA. This is particularly promising compared to immunocytokine-based or adjuvant-based cancer therapies, which often exhibit substantial toxicity and limit clinical translation[58–61]. Given the established clinical use of mRNA-LNP platforms, these findings further support the translational potential of NIK and IRF8 mRNA-based immunotherapies.

Remodeling of tumor microenvironment from IRF8 and NIK immunotherapy

We next examined the effect of IR-mRNA-LNPs on the immune microenvironment within tumors. For these initial evaluations, we selected the MB49 bladder cancer model because its comparatively low baseline immunogenicity provides a stringent setting to characterize treatment-driven immune remodeling[62]. Therefore, we implanted MB49 syngeneic tumors subcutaneously and, once the tumors reached ~100 mm^3 in size, we IT dosed IR-mRNA-LNPs (0.25 mg kg^{-1}) and collected the tumor, spleen and tumor-draining lymph nodes (TdLNs) on days 1 and 7 after injection to evaluate phenotypic and cellular changes associated with innate and adaptive immune responses (Fig. 3a). Day 1 following NIK and IRF8 mRNA-LNP treatment, we observed mild activation of both the cDC1 and cDC2 populations. Relative to FLuc treatment, IRF8 upregulated CD86 in cDC1s and cDC2s in the spleen and tumor. NIK treatment, meanwhile, only led to the upregulation of CD86 in tumor cDC1s, suggesting differential activity between the two mRNA constructs. (Fig. 3b, Extended Data Fig. 3a,b and Supplementary Fig. 10a,b). Moreover, 24 h after IRF8 treatment, cDC1 populations were elevated in TdLNs compared to controls. By day 7,

both NIK and IRF8 treatments increased cDC1 abundance in TdLNs (Fig. 3c and Supplementary Fig. 11b). We also observed selective expansion of cDC1s in the tumor and TdLN, with minimal effects observed in other APCs such as pDCs and cDC2s (Extended Data Fig. 3c,d and Supplementary Figs. 10 and 12). This expansion and activation of cDC1s is critical, as they are key drivers of antitumor $CD8^+$ T cell priming[44].

We then assessed the activation of both innate and adaptive lymphocytes following NIK and IRF8 mRNA-LNP treatment[63,64]. Both natural killer T (NKT) and γδT cells, which can kill tumor cells independently of classical MHC recognition, showed increased CD69 expression in tumors 24 h after treatment (Fig. 3d–i and Supplementary Fig. 11). This early activation was accompanied by greater accumulation of NKT and γδT cells in tumors compared to PBS and control mRNA groups. In addition to innate lymphocyte activation, NIK and IRF8 treatment enhanced adaptive immunity in the tumors. In TdLNs, no significant activation was observed in $CD4^+$ T cells across all treatment groups, whereas $CD8^+$ T cells showed upregulation of CD69, although activation was comparable to both IR-mRNA and FLuc treatment (Extended Data Fig. 3e). Within the tumor, $CD8^+$ T cells showed increased CD69 expression with IR-mRNA treatment relative to FLuc, while $CD4^+$ T cells were activated only in NIK-treated tumors (Extended Data Fig. 3f). By day 7, both NIK and IRF8 treatments increased infiltration of $CD8^+$ T cells and NIK also increased the number of $CD4^+$ T cells. Examining the phenotypes of these T cells, we observed an increase in the number of effector memory $CD8^+$ T cells in tumors compared to controls (Supplementary Fig. 13). Additionally, $CD4^+$ effector memory T cell numbers increased in NIK-treated tumors, whereas IRF8 did not affect $CD4^+$ T cell infiltration (Fig. 3j and Supplementary Fig. 13). Notably, both treatments resulted in a high ratio of $CD8^+$ to regulatory T cells (T_{reg} cells), indicating robust antitumor immunity without increasing immunosuppressive T_{reg} cells (Fig. 3k and Supplementary Fig. 11). Independent replication of these immunophenotyping studies exhibited consistent trends across experiments (Fig. 3, Extended Data Fig. 3 and Supplementary Fig. 10), supporting the reproducibility of the immune responses induced by IR-mRNA treatment. Overall, these results demonstrate that the innate immune engineering by NIK and IRF8 initiates antitumor adaptive immunity.

Elimination of established tumors and generation of long-lasting systemic immunity by mRNA-LNPs

Given the ability of IR-mRNA-LNPs to modulate the tumor immune microenvironment, we next sought to evaluate the therapeutic efficacy of these treatments in syngeneic tumor models. For these studies, we explored both IV and IT delivery strategies to compare their efficacy. Systemic delivery is clinically preferred because of its ease and for its ability to target both primary and metastatic tumors and induce systemic immunity[65,66]. However, systemic drug exposure at higher doses may cause adverse reactions. In contrast, IT administration can be more invasive but may reduce systemic therapeutic exposure while simultaneously providing higher levels within the tumor and surrounding lymphoid tissues for improved antigen trafficking[67–69].

As both administration routes have potential clinical advantages, we sought to understand whether IV and IT administration of LNPs could transfect key APC populations and enable IR-mRNA delivery to these cells. To examine transfection following IV administration, we administered Cre recombinase mRNA-LNPs to Ai14 mice, which express tdTomato following Cre expression. We then collected the spleen for flow cytometry analysis. Similarly, we examined mRNA expression in tumors following IT administration of tdTomato mRNA-LNPs and then collected the tumors for flow cytometry analysis. We observed that both IV and IT administration potentiated mRNA delivery to key DCs and macrophages in the spleen and tumor (Supplementary Figs. 14 and 15). These results suggest both administration routes enable IR-mRNA delivery to key APC cell subsets. Additionally, these results provided further insights into the phenotypic changes observed in Figs. 2 and 3.

Having confirmed the ability of IV and IT administration to deliver the IR-mRNAs to cell types of interest, we began therapeutic evaluations. We initially tested IR-mRNAs in two established subcutaneous (MC38, colorectal; MB49, bladder) syngeneic models to demonstrate broad applicability across tumor types. For evaluation in the MC38 model, we subcutaneously implanted tumors in C56BL/6J mice and performed weekly IT injections of IR-mRNA-LNPs or controls for 3 weeks (Fig. 4a). Mice treated with NIK or IRF8 mRNA-LNPs (0.25 mg kg^{-1}) showed significant tumor regression, while control groups receiving PBS or FLuc mRNA failed to control tumor growth. By day 20, complete tumor response was observed in 11 of 15 IRF8-treated and 11 of 16 NIK-treated mice, with the remaining showing delayed progression and prolonged survival. In contrast, control tumors rapidly progressed, reaching ~1,500 mm^3, necessitating euthanasia. This resulted in 73% (IRF8) and 69% (NIK) long-term survival, with all control mice euthanized by day 27 (Fig. 4b,c). Surviving mice rechallenged on the opposite flank on day 60 demonstrated robust memory responses, with 91% (NIK) and 82% (IRF8) rejecting tumors completely (Fig. 4d). IV administration of NIK or IRF8 mRNA (0.5 mg kg^{-1}, two doses on days 6 and 9) similarly suppressed tumor growth, with 60% of mice in both groups achieving complete response by day 15 (Supplementary Fig. 16). This led to 60% long-term survival, compared to 0% in mice treated with anti-PD1 or poly(I:C) (Supplementary Fig. 16b–g). Upon rechallenge on day 90, 100% of NIK-treated and 67% of IRF8-treated mice rejected tumor growth, confirming durable immune memory through systemic LNP administration (Supplementary Fig. 16h).

To provide additional insight into the mechanism by which these IR-mRNAs were inducing adaptive antitumor immunity, we performed antibody-mediated depletion of $CD8^+$ or $CD4^+$ T cells in mice bearing subcutaneous MC38 tumors, followed by treatment with IR-mRNA-LNPs. Depletion of $CD8^+$ T cells completely abolished the therapeutic efficacy of NIK and IRF8 mRNAs, with tumor progression comparable to PBS-treated controls. In contrast, depletion of $CD4^+$ T cells had only a modest effect and treated mice exhibited responses similar to wild-type controls. These results indicate that $CD8^+$ T cells are the primary mediators of the antitumor efficacy of IR-mRNA therapy (Supplementary Fig. 17). Additionally, this further supports the role

Fig. 3 | IR-mRNA treatment initiates immune cell activation and recruitment in tumors. a, Treatment scheme for evaluation of tumor immunophenotype following mRNA-LNP treatment. **b**, DC CD86 levels in TdLN, spleen and tumor after treatment. Data shown are the mean ± s.d. ($n = 4$ mice). **c**, cDC1 counts in the TdLN on days 1 and 7 following treatment. Data shown are the mean ± s.d. ($n = 4$ mice). **d**, Representative flow cytometry analysis of CD69 activation in γδT cells in tumors on day 1. **e**,**f**, Quantitative results showing the percentage of $CD69^+$ γδT cells in the tumor on day 1 (**e**) and number of $CD69^+$ γδT cells in the tumor on day 7 (**f**). Data shown are the mean ± s.d. ($n = 4$ mice for LNP-treated groups, $n = 3$ mice for PBS-treated groups). **g**, Representative flow cytometry analysis of CD69 activation of NKT in tumors on day 1. **h**,**i**, Quantitative results showing the percentage of $CD69^+$ NKT cells in the tumor on day 1 (**h**) and number of $CD69^+$ NKT cells in the tumor on day 7 (**i**). Data shown are the mean ± s.d. ($n = 4$ mice for LNP-treated groups, $n = 2$ or 3 mice for PBS-treated groups). **j**, $CD4^+$ (left) and $CD8^+$ (right) T cell counts in the tumors on day 7 after treatment. Data shown are the mean ± s.d. ($n = 4$ mice). **k**, Ratio of CD8 to T_{reg} cells in the tumor on day 7 following treatment. Data shown are the mean ± s.d. ($n = 3$ mice for PBS group, $n = 4$ mice for the FLuc and NIK/IRF8 groups). Statistical significance was analyzed using a one-way analysis of variance with a two-tailed Tukey's multiple-comparison test with a single pooled variance (**b**,**e**,**f**,**h**,**i**,**k**) or a repeated-measures two-way analysis of variance with a two-tailed Tukey's multiple-comparison test using a single pooled variance (**c**). These data are representative of three independent experiments. Panel **a** created in BioRender; Reed, K. https://biorender.com/k2g7bez (2026).

https://doi.org/10.1038/s41587-026-03115-2

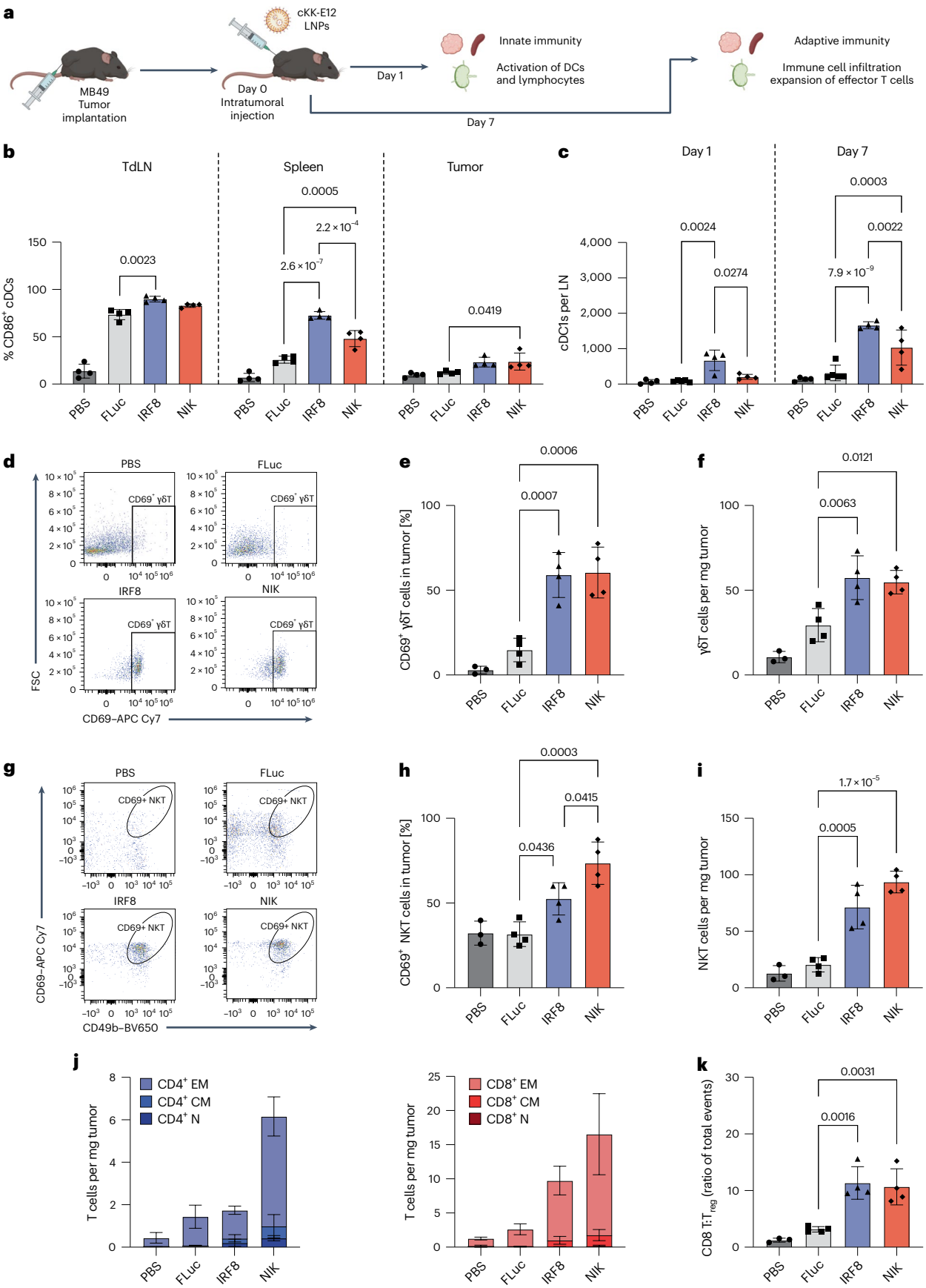

https://doi.org/10.1038/s41587-026-03115-2

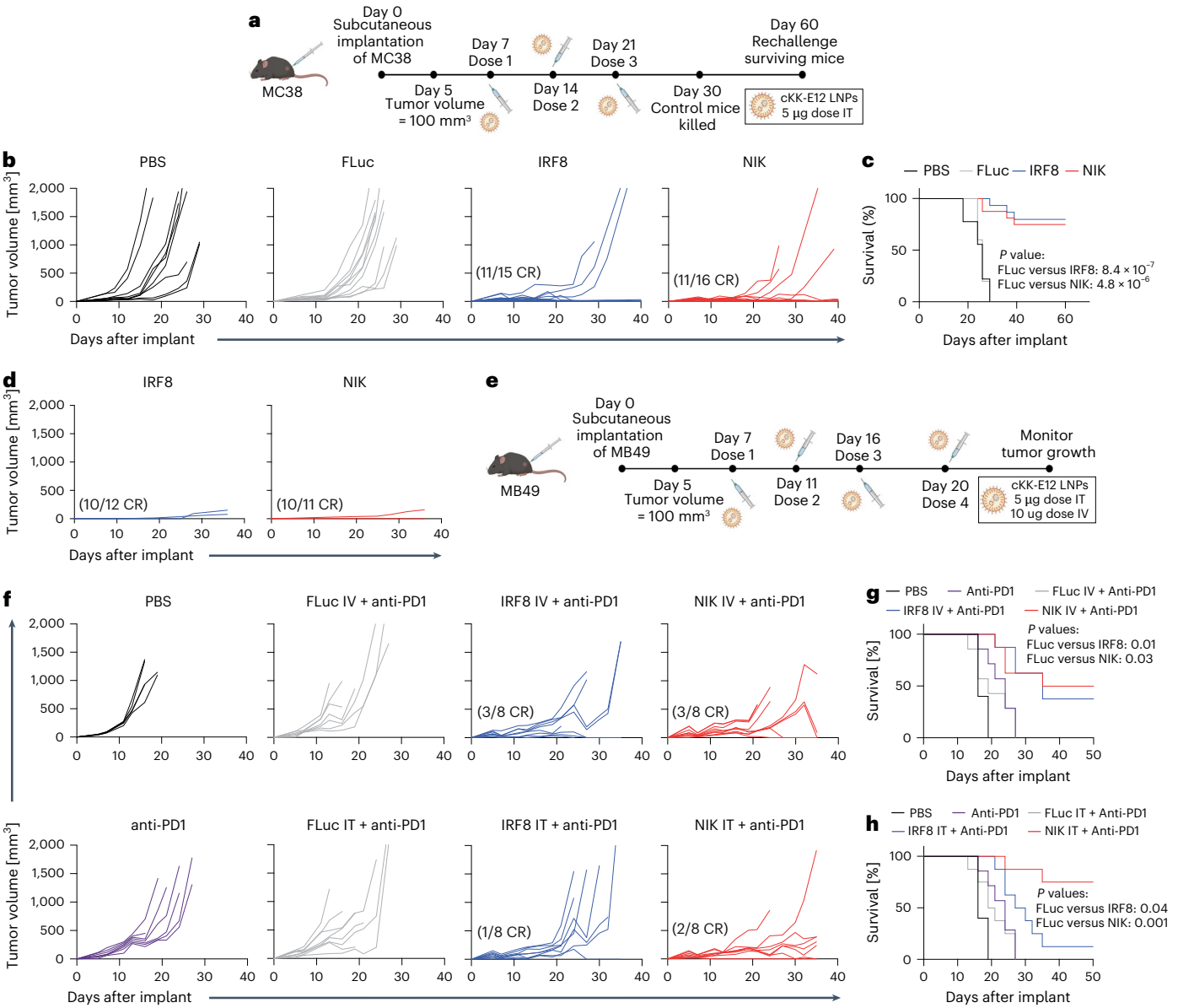

Fig. 4 | IR-mRNA-LNPs induce robust antitumor responses in aggressive syngeneic models. a, Schematic of IT treatment regimen for in vivo efficacy evaluation of NIK and IRF8 mRNA-LNP therapy with MC38 tumors. C5BL/6J mice were inoculated subcutaneously with 0.6×10^6 MC38 cells. When the tumor reached ~100 mm^3 in size, the lesion was injected with mRNA-LNPs. **b**,**c**, Tumor volumes (**b**) and survival curves (**c**) of different mouse cohorts ($n = 9$ mice for PBS, $n = 10$ mice for FLuc, $n = 15$ mice for IRF8 and $n = 16$ mice for NIK). **d**, Tumor growth curves following rechallenge of mice showing complete tumor rejection with MC38 cells on the opposite flank on day 60. **e**, Schematic illustrating the combination therapy approach using IV or IT administration of IR-mRNAs together with anti-PD1 in MB49 tumor models. C57BL/6J mice were subcutaneously inoculated with 0.2×10^6 MB49 cells. When tumors reached ~100 mm^3, mice received mRNA-LNPs (5 µg IT or 10 µg IV) in combination with anti-PD1 antibody (10 mg kg^{-1}, administered intraperitoneally twice per week). Treatment groups included PBS ($n = 5$), anti-PD1 alone ($n = 7$) and anti-PD1 combined with FLuc, IRF8 or NIK mRNA-LNPs ($n = 8$ each). **f**–**h**, Tumor growth curves for each treatment group (**f**) and survival curves following IV (**g**) and IT (**h**) mRNA-LNP administration ($n = 5$ mice for PBS only, $n = 7$ mice for anti-PD1 only and $n = 8$ mice for all other treatment groups). Statistical analysis was performed using the log-rank (Mantel–Cox) test with the Holm–Šídák correction for multiple comparisons (**c**,**g**,**h**). Panels **a** and **e** created in BioRender; Gupta, A. https://biorender.com/itm02de (2026).

of the IR-mRNAs in expanding and activating the cDC1 population to prime $CD8^+$ T cell responses.

Next, we investigated the cotreatment of IR-mRNA-LNPs with anti-PD1 antibody therapy to assess whether checkpoint inhibition could enhance the therapeutic efficacy of newly primed systemic T cell responses[70]. For these studies, C57BL/6J mice bearing MB49 tumors were treated with IR-mRNA-LNPs through both IV and IT administration in combination with intraperitoneally administered anti-PD1 checkpoint blockade (Fig. 4e). Untreated mice (PBS), mice treated with anti-PD1 alone and mice treated with a control mRNA-LNPs (FLuc) in combination with anti-PD1 were used as controls. Anti-PD1 monotherapy induced only modest delays in tumor growth and morbidity compared to PBS. The combination with FLuc LNPs did not result in any additional tumor inhibition (Fig. 4f). In contrast, both NIK and IRF8 mRNA-LNP treatments led to significant tumor growth suppression across all treated mice, with complete tumor responses observed with IRF8 and NIK treatment both IT and IV (Fig. 4g,h). For the NIK IT + anti-PD1 cohort, two of eight mice experienced complete tumor response, with no tumor growth up to day 50, while the other mice showed controlled tumor growth until the experiment

was terminated on day 50. Notably, even in the absence of anti-PD1 cotreatment, NIK and IRF8 monotherapies demonstrated potent antitumor activity, although they failed to induce complete responses in any animals (Supplementary Fig. 18). These results indicate that IR-mRNA-LNP treatments can elicit robust antitumor responses in aggressive, immunotherapy-refractory tumor models and hold promise for achieving durable therapeutic benefit when combined with checkpoint blockade.

We next evaluated the ability of IR-mRNA-LNPs to treat a metastatic model of cancer in mice. We IV injected (1×10^6) luciferase-expressing B16-F10 melanoma cells to establish lung metastases and tumor growth was monitored using bioluminescence imaging. Then, 1 week after tumor engraftment, mice received IV injections of LNPs encapsulating NIK, IRF8 or tdTomato (control) mRNA on days 5 and 9 (Fig. 5a). Notably, NIK-treated and IRF8-treated mice exhibited significantly reduced tumor growth compared to control groups (Fig. 5b,c). On day 15, the lungs were isolated to quantify tumor nodules and metastatic burden in the lung tissue using histopathology (Fig. 5d). Both NIK and IRF8 treatments significantly reduced lung metastases, with NIK achieving greater efficacy (Fig. 5e). Correspondingly, lung weight was significantly lower in treated groups (Supplementary Fig. 19), reflecting reduced tumor burden. Furthermore, immunohistochemistry (IHC) studies revealed 5.8-fold (NIK) and 4.5-fold (IRF8) increases in cytotoxic $CD8^+$ T cell infiltration in the tumors as compared to controls (Fig. 5f,g). Tumor cell proliferation was reduced ~12.4-fold (NIK) and ~5-fold (IRF8) compared to control mRNA (Fig. 5h,i). These findings support our hypothesis that these IR-mRNA-LNPs not only promote DC activation but subsequently induce effector T cell responses that suppress tumor growth. Overall, systemic NIK and IRF8 mRNA-LNPs elicited robust early antitumor effects and antimetastatic effects, highlighting their therapeutic potential on nonsuperficial tumors.

IRF8 and NIK mRNAs as adjuvants for cancer vaccines

After establishing that IR-mRNAs enhance systemic antitumor immunity and improve checkpoint inhibitor therapy, we investigated whether these mRNAs could generate durable, functional memory T cells capable of preventing or delaying tumor growth. As systemic delivery of NIK and IRF8 mRNA promotes IFN signaling and DC maturation in lymphoid tissues, we hypothesized that codelivery with a neoantigen-encoding mRNA could enhance antigen-specific effector and memory T cell responses capable of tumor rejection.

We immunized C57BL/6J mice with PBS, OVA mRNA alone (10 µg) or OVA mRNA codelivered with either NIK, IRF8 or FLuc (control) mRNA at a 1:1 ratio, keeping the total RNA dose constant (10 µg) (Methods). Vaccinations were conducted using a prime–boost regimen on days 0 and 14. Blood was collected from mice on day 7 and day 28 to evaluate the priming and expansion of antigen-specific $CD8^+$ T cells, followed by monitoring of blood $CD8^+$ T cells on days 60 and 90 to assess lasting memory response (Fig. 6a). On day 7, after the prime dose, there was already a significant increase in the fraction of circulating OVA-specific $CD8^+$ T cells with IRF8 (6.15%) and NIK (7.7%) compared to OVA^+ FLuc (4.15%) vaccination. After the boost dose, however, the differences became significantly higher; NIK + OVA and IRF8 + OVA showed 20% and 15% tetramer-positive $CD8^+$ T cells, respectively, compared to OVA alone (5.6%) or OVA + FLuc coadministered mice (4.7%) (Fig. 6b,c). Following vaccination, we assessed the longevity of this immune memory. At 2 months after the first dose, both mice immunized with NIK and IRF8 showed fourfold higher circulating $CD8^+$ T cells as compared to controls (mice treated with OVA and/or FLuc). Antigen-specific $CD8^+$ T cells remained persistent even 3 months after vaccination with NIK and IRF8, showing 12% and 13% tetramer-positive $CD8^+$ T cells, respectively. In contrast, control mice showed minimal remaining $CD8^+$ T cells by this time point (Fig. 6b,c). We also investigated potential synergy between NIK and IRF8 by coadministering NIK + IRF8 + OVA but we did not observe an improvement in the generation of OVA-specific $CD8^+$ T cells (Supplementary Fig. 20a).

We then evaluated the protective efficacy of this prophylactic vaccination using a B16-OVA subcutaneous melanoma model. Then, 90 days after the first dose, OVA-expressing B16-F10 cells were subcutaneously implanted in the immunized mice. Mice treated with OVA (alone) and FLuc (coadministered) showed a slight delay in tumor growth; however, this did not significantly improve their survival probability compared to unvaccinated mice (Fig. 6d,e). Both NIK-treated and IRF8-treated mice showed complete rejection in five of five treated mice (Fig. 6d,e). These results indicate that these IR-mRNAs can be used as adjuvants to prophylactic cancer vaccines to enhance the generation of long-lived, functional $CD8^+$ T cells.

Lymphoid-targeted delivery of IRF8 and NIK enhances their cancer vaccine adjuvant effects

Although these experiments demonstrated the potential of NIK and IRF8 as cancer vaccine adjuvants, the LNPs used for this experiment primarily yield mRNA expression in the liver. We hypothesized that we could further enhance cancer vaccine potency by combining the adjuvant effects of our IR-mRNAs with targeted RNA delivery to lymphoid organs such as the spleen, where APCs are in proximity to T cells[66,71]. To identify an LNP formulation that targets mRNA delivery to the spleen, we screened a combinatorial library of 100 ionizable lipids previously reported by our lab[72]. We formulated FLuc mRNA into LNPs with these ionizable lipids, injected them IV and then evaluated biodistribution using bioluminescence imaging. From our initial screen, we identified the ionizable lipid AMG56, which gave relatively specific and potent mRNA expression in the spleen. This ionizable lipid consists of a spirocyclic diamine headgroup with branched tails (Extended Data Fig. 4a). To further improve mRNA delivery to splenic APCs, we synthesized an additional 20 ionizable lipids by varying the tail length. We screened them to identify the most potent vehicles for splenic delivery (Supplementary Methods and Extended Data Fig. 4b). All of these lipids demonstrated enhanced spleen delivery compared to the standard control LNP (cKK-E12), with AMG514 achieving ~4-fold higher delivery (Extended Data Fig. 4c,d).

Both cKK-E12 and AMG514 mediated mRNA transfection in splenic DCs and macrophages (Extended Data Fig. 4e), although AMG514 showed significantly greater transfection efficiency in these key APC populations. To investigate the mechanism of spleen targeting of AMG514, we investigated the LNP protein corona following incubation with plasma. We found that these LNPs had enriched levels

Fig. 5 | IR-mRNAs generate systemic antitumor immunity exhibit therapeutic efficacy in metastatic tumors. a, Schematic of the systemic treatment regimen for in vivo efficacy evaluation of NIK and IRF8 mRNA therapy in metastatic B16-F10 tumors. B6 albino mice were inoculated systemically with 1×10^6 B16-F10-FLuc cells, followed by IV administration of mRNA-LNPs on days 5 and 9 after tumor injection. **b**,**c**, B16-F10-Luc tumor growth in lungs monitored using IVIS imaging ($n = 10$ mice per group). Data shown are the mean ± 95% confidence interval. **d**, Representative H&E staining of treated and control lungs. **e**, Metastatic lung burden shown as a percentage of lung tissue after NIK or IRF8 treatment. Data shown are the mean ± s.d. ($n = 10$ mice). **f**,**g**, Representative immunofluorescence images of tumor-infiltrating $CD8^+$ T cells (**f**) and quantified results (**g**). Scale bar, 40 µm. Data shown are the mean ± s.d. ($n = 5$ mice). **h**,**i**, Representative IHC images of lung tissue stained for Ki67 (**h**) and quantified results (**i**). Scale bar, 100 µm. Data shown are the mean ± s.d. ($n = 5$ mice). Statistical analysis was performed using a one-way analysis of variance with a two-tailed Tukey's multiple-comparison test with a single pooled variance (**e**) or a Brown–Forsythe and Welch analysis of variance with a two-tailed Dunnet T3 multiple-comparison test (**g**,**i**). Panel **a** created in BioRender; Reed, K. https://biorender.com/mvkrd3x (2026).

https://doi.org/10.1038/s41587-026-03115-2

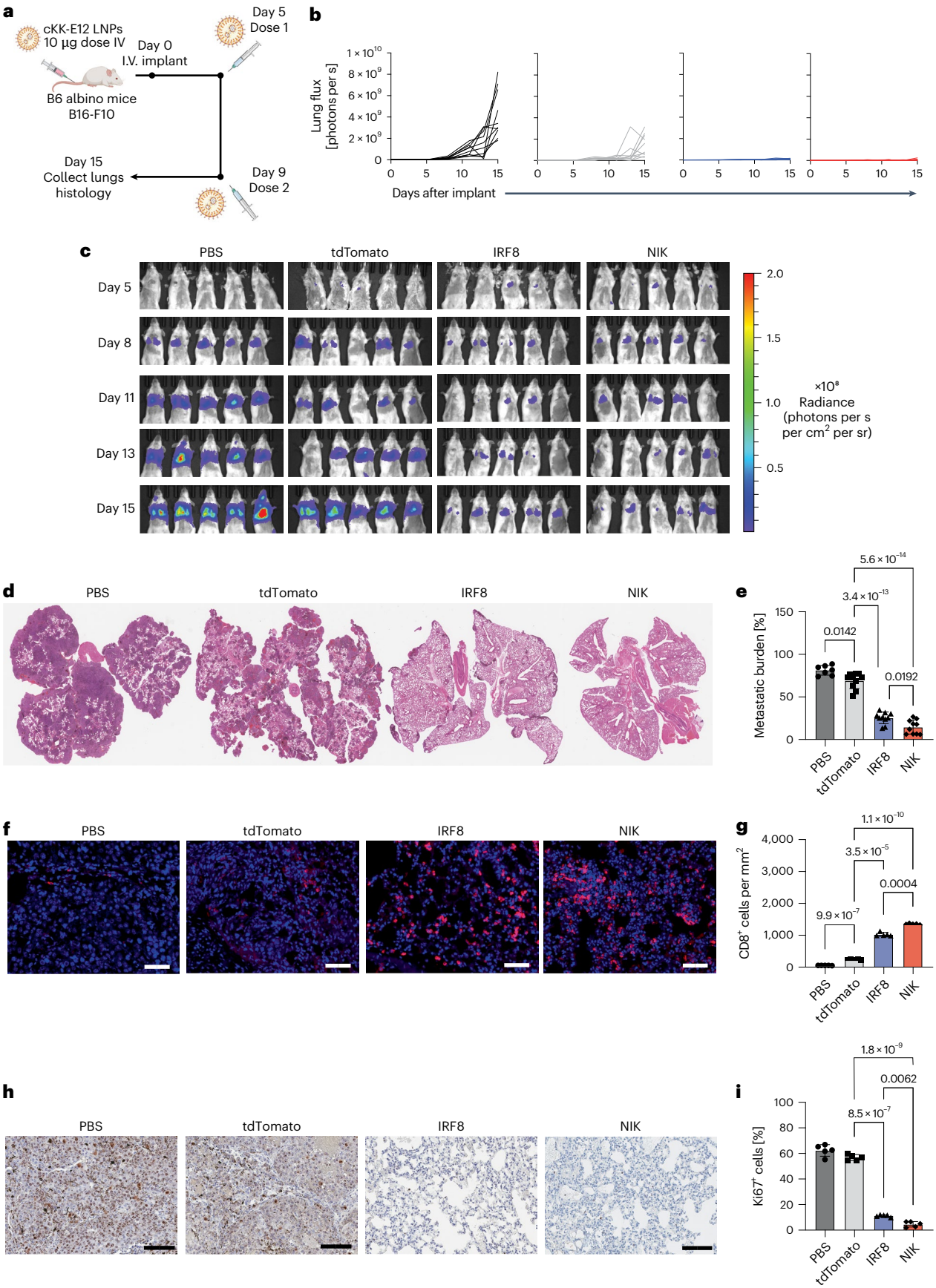

of integrin-binding and phagocytosis-associated proteins on their surface, including vitronectin (30.3%), prothrombin and coagulation factors (24%) and fibrinogen (9.3%), which collectively engage receptors abundantly expressed on splenic macrophages and DCs[73–75]. Additional lower-abundance but high-potency opsonins—such as thrombospondin 1 (1.0%) and ApoA-IV (6.9%)—further support scavenger-receptor-mediated internalization by myeloid cells (Supplementary Fig. 21a)[76,77]. Together, this corona profile promotes rapid uptake by phagocytic immune populations and accounts for the predominant localization of AMG514 LNPs to the spleen and their efficient delivery to macrophages and DC subsets. Notably, this pattern differs from liver-tropic LNPs, whose coronas are typically dominated by ApoE and albumin—components largely absent here. Consistent with this distinction, AMG514 LNPs exhibit a pKa of ~7.5, markedly higher than the ~6.5 pKa characteristic of liver-tropic formulations (Supplementary Fig. 21b)[78].

We next investigated whether these spleen-tropic LNPs could enhance adaptive immune responses by codelivering IR-mRNAs and neoantigen-encoding OVA mRNA to the splenic lymphoid compartments. C57BL/6J mice were immunized with PBS, AMG514-formulated OVA mRNA alone (3 µg) or OVA mRNA codelivered with NIK mRNA at a 1:1 ratio (total RNA dose 3 µg), formulated using either AMG514 or cKK-E12 (Fig. 6f). We selected a lower dose for these experiments to evaluate the potential for improved splenic delivery to increase potency. Blood was collected from vaccinated mice on days 7 and 28 to assess the priming and expansion of antigen-specific $CD8^+$ T cells. Notably, AMG514-formulated NIK + OVA generated 15% tetramer-positive $CD8^+$ T cells, significantly higher than cKK-E12-formulated NIK + OVA (6%) (Fig. 6g,h). Additionally, NIK codelivery once again showed superior $CD8^+$ T cell priming relative to mice vaccinated with OVA only.

Given the strong T cell responses from AMG514 LNPs with NIK mRNA (Fig. 6g,h), we challenged vaccinated mice with B16-OVA tumor cells on day 35 and monitored tumor growth. Mice immunized with AMG514 OVA only showed delayed tumor growth compared to untreated PBS controls and one mouse showing complete tumor rejection (Fig. 6i,j). Mice vaccinated with NIK + OVA showed delays in tumor growth and higher rejection rates. cKK-E12 LNPs gave complete rejection in three of five treated mice, while AMG514 LNPs showed an increased albeit not statistically significant complete rejection in five of five mice (Fig. 6i,j). These studies demonstrate the utility of an optimized mRNA delivery vehicle in combination with these IR-mRNAs to enhance tumor-specific immune responses.

IR-mRNAs as adjuvants to infectious disease mRNA vaccines

Given the performance of NIK and IRF8 as cancer vaccine adjuvants, we hypothesized that codelivery of either NIK or IRF8 mRNA with a viral antigen-encoding mRNA could extend the application of these IR-mRNAs to infectious disease vaccines. mRNA vaccines for infectious diseases have emerged as a transformative platform, exemplified by their rapid development and success against COVID-19 (ref. 79). mRNA vaccines consist of mRNA and LNPs, which can activate innate immune pathways to enhance adaptive immunity[10]. For example, the BNT162b2 COVID-19 vaccine was shown to activate the MDA5 and IFNAR1 signaling pathways in APCs, driving the resultant cellular and humoral immunity[80]. While these formulations can drive antigen-specific immune responses, there remains opportunities to further enhance the potency of mRNA vaccines for infectious diseases. IR-mRNAs induce type I IFN secretion and IL-12 production (Fig. 1) while simultaneously promoting DC maturation. Together, these effects drive a Th1-type response that enhances the generation of robust adaptive immunity[39].

To evaluate the potential of the IR-mRNAs as adjuvants to infectious disease mRNA vaccines, we vaccinated BALB/cJ mice with hemagglutinin (H3) (A/Tasmania/503/2020 H3N2) mRNA alone or combined with IRF8, NIK or a control (FLuc) mRNA using a prime–boost regimen on days 0 and 21 (Extended Data Fig. 5a). Antibody titers were measured to assess humoral responses. Similarly, mice were vaccinated with SARS-CoV-2 spike mRNA under the same conditions. In both antigen models, vaccines with adjuvants (with NIK or IRF8) elicited a fourfold increase in IgG titers compared to vaccines without (Supplementary Fig. 22).

Building on these results, we further performed vaccination studies in C57BL/6J mice, a Th1-biased model. Mice were again vaccinated with H3 mRNA in cKK-E12 LNPs either alone or with cKK-E12 LNPs encoding IRF8, NIK or FLuc mRNA (Extended Data Fig. 5a). We first examined T cell responses by performing an IFNγ ELISpot analysis of peptide-stimulated splenocytes. This revealed a robust Th1-biased cellular response, with MHC-I peptide pools eliciting higher responses than MHC-II (Extended Data Fig. 5b–d). Like the cancer vaccine results, NIK and IRF8 used adjuvant to vaccines induced substantially stronger T cell responses. The number of MHC-I peptide-induced IFNγ spots with IRF8 and NIK used as adjuvants increased 13.3-fold and 14.4-fold, respectively, compared to the H3-only control (Extended Data Fig. 5b,c). We additionally analyzed the cytokines secreted from the peptide-stimulated splenocytes and observed upregulation of a diverse range of Th1-associated and Th2-associated cytokines, including GM-CSF, IL-2, IL-5 and IL-10, relative to H3 + FLuc vaccination (Extended Data Fig. 5e). This provides further confirmation of the strong cellular responses induced by IR-mRNAs as adjuvants. We additionally examined the binding antibody titers on day 35 and found that the vaccines used with adjuvant induced 4.5-fold (IRF8) and 4.9-fold (NIK) higher antibody titers than controls (Extended Data Fig. 5f). We also investigated potential synergy between NIK and IRF8 by coadministering NIK + IRF8 + H3 mRNAs but we did not observe an improvement in the generation of H3-binding antibodies (Supplementary Fig. 20b). Overall, these results demonstrate that NIK and IRF8 could potentially be extended to infectious disease vaccines to enhance their efficacy.

Discussion

Engineering myeloid cells from an immature state to a mature, professional antigen-presenting phenotype has the potential to enhance

Fig. 6 | IR-mRNAs boost $CD8^+$ T cell response for cancer vaccines. a, Schematic overview of the timeline for cancer vaccination, blood collection and T cell analysis, followed by tumor inoculation. Mice were immunized on days 0 and 14 with OVA (10 µg) and OVA + FLuc, NIK or IRF8 (5 + 5 µg) mRNA-LNP. Blood samples were collected on days 7, 28, 60 and 90 for quantification of OVA-specific $CD8^+$ T cells. Vaccinated mice were inoculated with 0.3×10^6 B16-Ova cells subcutaneously on day 90 and monitored for tumor growth. **b**,**c**, Representative flow cytometry analysis of the percentages of circulating OVA-specific $CD8^+$ T cells (**b**) and quantified results (**c**). Data shown are the mean ± s.d. ($n = 5$ mice). **d**,**e**, Tumor volume (**d**) and survival curves (**e**) following B16-F10 challenge. **f**, Schematic overview of the timeline for cancer vaccination using spleen-tropic LNPs (AMG514) and control LNPs (cKK-E12). Mice were immunized on days 0 and 14 with AMG514 (OVA, 3 µg) or AMG514 and cKK-E12 (1.5 µg OVA + 1.5 µg NIK) mRNA-LNP. Blood samples were collected on days 7 and 28 for quantification of OVA-specific $CD8^+$ T cells, followed by B16-OVA cell inoculation for tumor challenge on day 35. **g**,**h**, Representative flow cytometry analysis of the percentages of circulating OVA-specific $CD8^+$ T cells (**g**) and quantified results (**h**). Data shown are the mean ± s.d. ($n = 5$ mice). **i**,**j**, Tumor growth curves for different treatment groups (**i**) and survival curves (**j**) following tumor challenge ($n = 5$ mice). Statistical significance was analyzed using a two-way analysis of variance with a two-tailed Tukey's multiple-comparison test with individual variances for each comparison (**c**), two-way analysis of variance with a two-tailed Tukey's multiple-comparison test with a single pooled variance (**h**) or a log-rank (Mantel–Cox) test with the Holm–Šídák correction for multiple comparisons (**e**). Panels **a** and **f** created in BioRender; Gupta, A. https://biorender.com/7eb26yu (2026).

https://doi.org/10.1038/s41587-026-03115-2

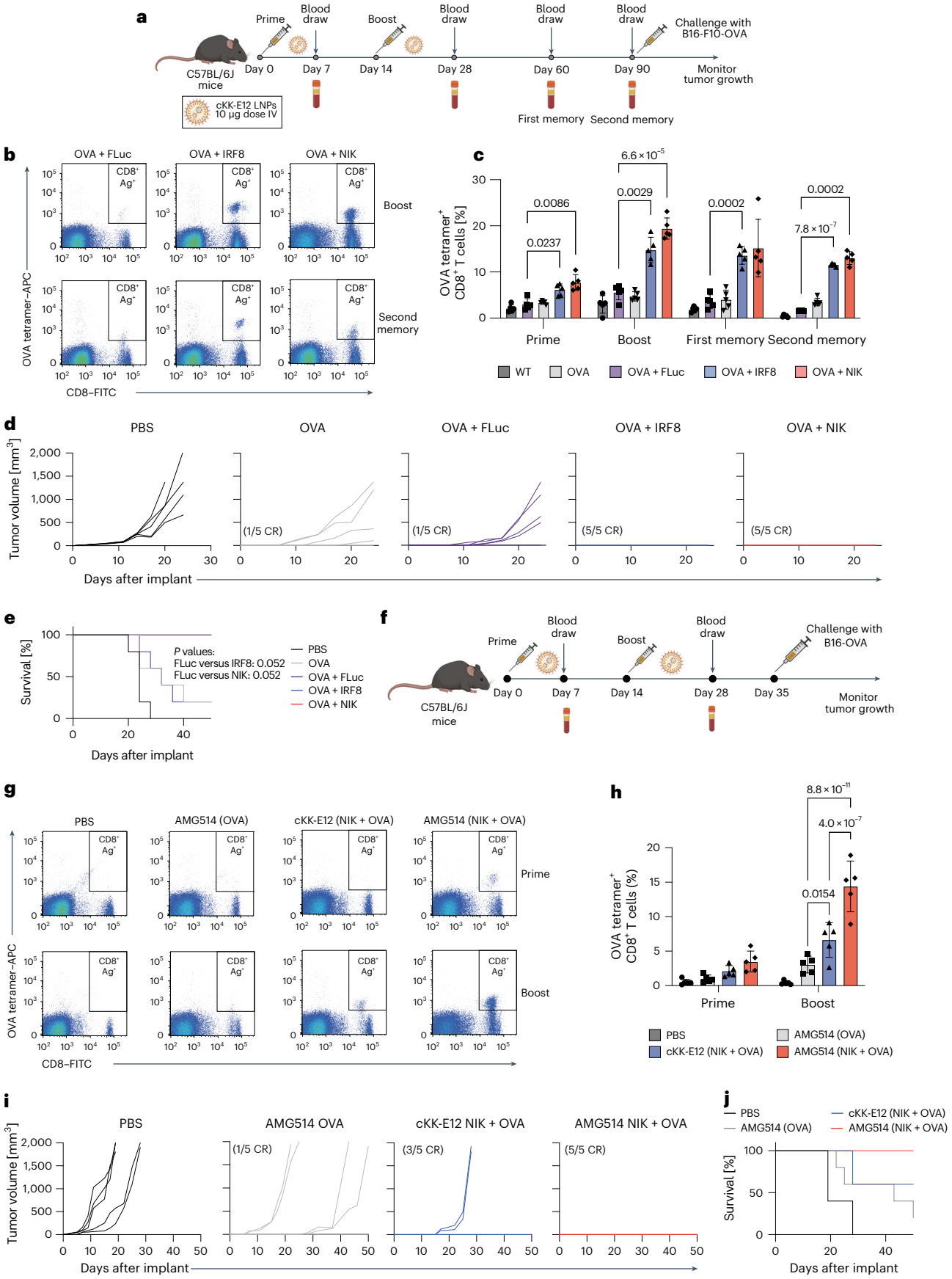

immune responses against pathogenic or tumor-associated antigens. Delivery of mRNAs encoding intracellular cytosolic regulators remains largely underexplored for APC modulation. Here, we used mRNA-LNPs to deliver the IR-mRNAs (NIK and IRF8) driving APC maturation to generate stronger adaptive immune responses in the context of cancer immunotherapy and infectious disease vaccination. Using flow cytometry and scRNA-seq, we demonstrated that IR-mRNA treatment induces cDC1-like transcriptional and phenotypic features in immature BMDCs. This was evidenced by the upregulation of key maturation markers (*Cd40*, *Cd80* and *Cd86*) and genes associated with antigen presentation and T cell activation (*Ctsc*, *Nlrc5*, *Stat3* and *Il12b*) (Fig. 1). IR-mRNA treatment also induced protein-level expression of proinflammatory cytokines, including IL-12 and IFN-I, which enhance T cell recruitment and activation. Importantly, RNA-seq revealed that IR-mRNAs upregulated lineage-defining transcription factors such as *Batf3*, *Spi1* and *Irf8*. In parallel, these cells exhibited increased expression of surface markers (MHC-II, CD8, CD103 and XCR1) characteristic of cDC1s, reflecting enhanced cDC1-like features (Fig. 1 and Supplementary Figs. 3 and 5). Notably, a moderate expansion of the cDC2 cluster was observed upon IR-mRNA treatment in scRNA-seq analysis (Fig. 1h,i). The transcription shift was less significant than observed in cDC1 phenotypes (Fig. 1j,i). In vivo, we observed expansion and activation of cDC1s but the expansion of cDC2s was less significant, suggesting the IR-mRNAs had a stronger effect on cDC1s in the context of the tumor microenvironment. These findings suggest that IR-mRNA treatment preferentially enhances cDC1 responses within the tissue microenvironment and that in vitro transcriptional changes do not necessarily predict proportional expansion or infiltration in vivo (Extended Data Fig. 3c and Supplementary Fig. 12).

These results demonstrate that, although NIK and IRF8 initiate distinct signaling cascades, both ultimately amplify transcriptional programs associated with cDC1 maturation, antigen processing and IFN-I responsiveness. This convergence on a shared cross-presenting phenotype provides a mechanistic explanation for their similar antitumor effects. Thus, IR-mRNAs can act through complementary upstream pathways that funnel into a unified cDC1-driven immune response. These observations were recapitulated by cDC1 activation and expansion in the TdLNs and tumors of syngeneic tumor-bearing mice following IR-mRNA-LNP treatment (Fig. 3 and Supplementary Fig. 12). Meanwhile, we did not observe expansion of other tumor-infiltrating APC populations such as cDC2 and pDCs or macrophages (Supplementary Fig. 12). IR-mRNA treatment was also accompanied by rapid recruitment of γδT cells and NKT cells, followed by infiltration of $CD8^+$ T cells (Fig. 3). Notably, cKK-E12 mRNA-LNPs were taken up predominantly by APCs (~35%), with additional transfection of tumor cells (~15%) and stromal cells (~5%), suggesting that IT delivery directly modulates APC subsets, while transient NIK or IRF8 expression in tumor and stromal compartments may also contribute to remodeling of the tumor microenvironment (Supplementary Fig. 15). IV delivery of LNPs showed mRNA transfection predominantly in APCs in the spleen, specifically DCs and macrophages, with minimal delivery to non-APC populations (Supplementary Fig. 14). These findings indicate that APCs are the primary cellular targets of IR-mRNA delivery in vivo and, therefore, the principal immune populations directly engineered to initiate antitumor immunity. Immunostimulated APCs secrete IFN-Is and proinflammatory cytokines, which in turn drive secondary activation of lymphocytes and other leukocytes in the tumor and the TdLN (NKT, γδ T, $CD4^+$ and $CD8^+$ T cell activation; Fig. 3e,h and Extended Data Fig. 3e,f). This cascade is further reflected in the increased infiltration of effector lymphocytes ($CD4^+$, $CD8^+$, NKT and γδT cells), $Ly6C^{high}$ monocytes and granulocytes in tumors—cell types known to contribute to antitumor responses (Supplementary Fig. 12).

This immune remodeling resulted in potent antitumor responses across multiple syngeneic cancer models following both IT and IV administration, highlighting the platform's versatility for treating accessible lesions, as well as metastatic or visceral malignancies. Notably, these responses were durable and conferred protection against tumor rechallenge, indicative of long-term antitumor immunity (Figs. 4 and 5). Furthermore, coadministration of IR-mRNAs with anti-PD1 immune checkpoint blockade (ICB) therapy significantly improved tumor regression and long-term survival in immunologically 'cold' MB49 tumors (Fig. 4). These IR-mRNAs may, therefore, hold promise as a complementary strategy to existing ICB therapeutics, which often fail because of insufficient preexisting antigen presentation and T cell priming. Furthermore, depletion of $CD8^+$ T cells resulted in ablation of the therapeutic efficacy of these IR-mRNAs, further supporting a cDC1-mediated antitumor immune response (Supplementary Fig. 17).

In addition to potentiating antitumor responses alone or in combination with ICB, these IR-mRNAs can also be used in combination with chosen antigens as adjuvants to significantly augment immune responses for both cancer and infectious disease vaccines. Coadministration of IR-mRNAs with OVA enhanced $CD8^+$ T cell responses, resulting in ~20% circulating antigen-specific $CD8^+$ T cells, 1 month after vaccination, with sustained response showing ~13% circulating T cells in the blood 3 months after vaccination, highlighting both robust induction and sustained T cell immunity. Notably, all vaccinated mice completely rejected tumor rechallenge 3 months after the initial immunization, demonstrating the durability and potency of the immune response (Fig. 6). To further enhance the efficacy of the cancer vaccine strategy, we developed ionizable lipids (AMG514) designed to improve mRNA delivery to splenic DCs and macrophages (Extended Data Fig. 4). AMG514 significantly amplified vaccine-induced immune responses, resulting in effective tumor growth inhibition at lower doses. These findings underscore the importance of optimizing both adjuvant potency and delivery efficiency to maximize the therapeutic potential of cancer vaccines. Moreover, IR-mRNA as adjuvant to flu mRNA vaccines elicited significantly stronger humoral (~5-fold) and cellular (~15-fold) responses as compared to antigen alone (H3 mRNA) (Extended Data Fig. 5). Another advantage of this mRNA-LNP platform is the ability to precisely control the relative doses of antigen and adjuvant (IRF8 or NIK) mRNA to enable reproducible responses across a range of antigens and providing a tunable strategy essential for shaping the desired adaptive immunity.

NIK activates the noncanonical NF-κB pathway downstream of receptors such as CD40 and BAFF-R, driving DC cross-priming and key immunostimulatory cytokines. We previously showed that NIK loss in DCs eliminates anti-PD1 efficacy and impairs $CD8^+$ T cell priming, establishing NIK as essential for adaptive antitumor immunity[21,36]. Although chronic or genetically sustained NIK overactivation can lead to aberrant noncanonical NF-κB signaling associated with inflammation and tumor progression, this biology fundamentally differs from the transient and tightly regulated expression achieved through mRNA-LNP delivery[81]. Under physiological conditions, NIK protein is continuously targeted for degradation and accumulates only upon specific receptor engagement or pharmacologic NIK stabilization (for example, cIAP inhibition). Thus, transient NIK expression from mRNA closely resembles normal physiological kinetics rather than the chronic, pathological activation linked to oncogenesis[20]. Consistent with this, NIK and IRF8 mRNA-LNP vaccination did not result in sustained weight loss, behavioral abnormalities or liver or spleen pathology (Supplementary Figs. 8 and 9). Even at doses up to threefold higher than the therapeutic dose, NIK-treated mice showed weight curves comparable to FLuc mRNA-LNP controls and fully recovered by day 4. Serum chemistry markers (ALT and AST) remained within normal ranges, further supporting a favorable tolerability profile (Extended Data Fig. 2). Moreover, mice achieving complete tumor regression (Figs. 4 and 6) upon IR-mRNA vaccination and therapy were monitored for up to 1 year and exhibited no delayed toxicity or behavioral abnormalities. These findings indicate

that our approach harnesses the immunostimulatory benefits of NIK and IRF8 while avoiding mechanisms associated with chronic pathway dysregulation.

These findings provide a robust preclinical foundation for the efficacy and tolerability of IR-mRNA-based immunotherapy; however, opportunities for further investigation remain to facilitate clinical translation. Studies in humanized models and patient-derived organoids will enable rigorous assessment of IR-mRNA function across the heterogeneous and immunosuppressive architecture of human tumors. Integration with clinically relevant or individual-specific neoantigens could further extend the translational potential of IR-mRNAs for cancer vaccination. Evaluation in orthotopic and highly immunosuppressive tumor models, such as pancreatic cancer and glioblastoma, will be important to define therapeutic performance in more stringent and clinically relevant settings characterized by limited APC activity and dominant myeloid-driven suppression. Lastly, moving beyond murine models to evaluate the pharmacokinetics and safety profile of these mRNA-LNPs in larger animal models will be essential.

Overall, we demonstrated that IR-mRNAs encoding cytosolic immune-remodeling factors initiate cascaded signaling pathways that engineer the tumor microenvironment and direct immune cell fate, ultimately enhancing therapeutic efficacy. Their capacity to improve antigen presentation and promote lymphocyte infiltration, effectively converting cold tumors into hot, positions them as strong candidates to complement existing ICB therapeutics in clinical settings. Moreover, IR-mRNAs also demonstrate substantial potential to amplify antigen-specific responses in both cancer and infectious disease vaccines. In cancer vaccination, their ability to elicit unprecedented levels of antigen-specific $CD8^+$ T cells supports their use in personalized vaccines targeting individual-derived neoantigens. Additionally, by enhancing both humoral and cellular immunity, IR-mRNAs may serve as potent adjuvants for next-generation infectious disease vaccines, especially in vulnerable populations such as older adults or individuals with compromised immune systems.

Online content

Any methods, additional references, Nature Portfolio reporting summaries, source data, extended data, supplementary information, acknowledgements, peer review information; details of author contributions and competing interests; and statements of data and code availability are available at https://doi.org/10.1038/s41587-026-03115-2.

References

1. Jhunjhunwala, S., Hammer, C. & Delamarre, L. Antigen presentation in cancer: insights into tumour immunogenicity and immune evasion. *Nat. Rev. Cancer* **21**, 298–312 (2021).
2. Chen, D. S. & Mellman, I. Oncology meets immunology: the cancer–immunity cycle. *Immunity* **39**, 1–10 (2013).
3. Galassi, C., Chan, T. A., Vitale, I. & Galluzzi, L. The hallmarks of cancer immune evasion. *Cancer Cell* **42**, 1825–1863 (2024).
4. Emens, L. A. et al. Challenges and opportunities in cancer immunotherapy: a Society for Immunotherapy of Cancer (SITC) strategic vision. *J. Immunother. Cancer* **12**, e009063 (2024).
5. Hegde, P. S. & Chen, D. S. Top 10 challenges in cancer immunotherapy. *Immunity* **52**, 17–35 (2020).
6. Sharma, P. & Allison, J. P. The future of immune checkpoint therapy. *Science* **348**, 56–61 (2015).
7. Hou, X., Zaks, T., Langer, R. & Dong, Y. Lipid nanoparticles for mRNA delivery. *Nat. Rev. Mater.* **6**, 1078–1094 (2021).
8. Liu, C. et al. mRNA-based cancer therapeutics. *Nat. Rev. Cancer* **23**, 526–543 (2023).
9. Pardi, N., Hogan, M. J., Porter, F. W. & Weissman, D. mRNA vaccines—a new era in vaccinology. *Nat. Rev. Drug Discov.* **17**, 261–279 (2018).
10. Gupta, A., Rudra, A., Reed, K., Langer, R. & Anderson, D. G. Advanced technologies for the development of infectious disease vaccines. *Nat. Rev. Drug Discov.* **23**, 914–938 (2024).
11. Hewitt, S. L. et al. Durable anticancer immunity from intratumoral administration of IL-23, IL-36γ, and OX40L mRNAs. *Sci. Transl. Med.* **11**, eaat9143 (2019).
12. Li, Y. et al. Multifunctional oncolytic nanoparticles deliver self-replicating IL-12 RNA to eliminate established tumors and prime systemic immunity. *Nat. Cancer* **1**, 882–893 (2020).
13. Brook, B. et al. Adjuvantation of a SARS-CoV-2 mRNA vaccine with controlled tissue-specific expression of an mRNA encoding IL-12p70. *Sci. Transl. Med.* **16**, eadm8451 (2025).
14. Saxton, R. A., Glassman, C. R. & Garcia, K. C. Emerging principles of cytokine pharmacology and therapeutics. *Nat. Rev. Drug Discov.* **22**, 21–37 (2023).
15. Stetson, D. B. & Medzhitov, R. Type I interferons in host defense. *Immunity* **25**, 373–381 (2006).
16. van Herpen, C. M. et al. Pharmacokinetics and immunological aspects of a phase Ib study with intratumoral administration of recombinant human interleukin-12 in patients with head and neck squamous cell carcinoma: a decrease of T-bet in peripheral blood mononuclear cells. *Clin. Cancer Res.* **9**, 2950–2956 (2003).
17. Eton, O. et al. Phase I trial of subcutaneous recombinant human interleukin-2 in patients with metastatic melanoma. *Cancer* **95**, 127–134 (2002).
18. Leonard, J. P. et al. Effects of single-dose interleukin-12 exposure on interleukin-12-associated toxicity and interferon-γ production. *Blood* **90**, 2541–2548 (1997).
19. Chen, D. S. & Mellman, I. Elements of cancer immunity and the cancer–immune set point. *Nature* **541**, 321–330 (2017).
20. Sun, S.-C. The non-canonical NF-κB pathway in immunity and inflammation. *Nat. Rev. Immunol.* **17**, 545–558 (2017).
21. Garris, C. S. et al. Successful anti-PD-1 cancer immunotherapy requires T cell-dendritic cell crosstalk involving the cytokines IFN-γ and IL-12. *Immunity* **49**, 1148–1161 (2018).
22. Katakam, A. K. et al. Dendritic cells require NIK for CD40-dependent cross-priming of $CD8^+$ T cells. *Proc. Natl Acad. Sci. USA* **112**, 14664–14669 (2015).
23. Durai, V. et al. Cryptic activation of an Irf8 enhancer governs cDC1 fate specification. *Nat. Immunol.* **20**, 1161–1173 (2019).
24. Grajales-Reyes, G. E. et al. Batf3 maintains autoactivation of Irf8 for commitment of a $CD8\alpha^+$ conventional DC clonogenic progenitor. *Nat. Immunol.* **16**, 708–717 (2015).
25. Lança, T. et al. IRF8 deficiency induces the transcriptional, functional, and epigenetic reprogramming of cDC1 into the cDC2 lineage. *Immunity* **55**, 1431–1447 (2022).
26. Anderson, D. A., Dutertre, C.-A., Ginhoux, F. & Murphy, K. M. Genetic models of human and mouse dendritic cell development and function. *Nat. Rev. Immunol.* **21**, 101–115 (2021).
27. Del Prete, A. et al. Dendritic cell subsets in cancer immunity and tumor antigen sensing. *Cell. Mol. Immunol.* **20**, 432–447 (2023).
28. Varfolomeev, E. et al. IAP antagonists induce autoubiquitination of c-IAPs, NF-κB activation, and TNFα-dependent apoptosis. *Cell* **131**, 669–681 (2007).
29. West, A. C. et al. The SMAC mimetic, LCL-161, reduces survival in aggressive MYC-driven lymphoma while promoting susceptibility to endotoxic shock. *Oncogenesis* **5**, e216 (2016).
30. Ascic, E. et al. In vivo dendritic cell reprogramming for cancer immunotherapy. *Science* **386**, eadn9083 (2025).
31. Zimmermannova, O. et al. Restoring tumor immunogenicity with dendritic cell reprogramming. *Sci. Immunol.* **8**, eadd4817 (2025).
32. Cliff, E. R. S. et al. High cost of chimeric antigen receptor T-cells: challenges and solutions. *Am. Soc. Clin. Oncol. Educ. Book* **43**, e397912 (2023).

33. Dropulić, B. CAR-T and cellular gene therapies are too expensive. *Nat. Med.* **30**, 2714 (2024).
34. Hinderer, C. et al. Severe toxicity in nonhuman primates and piglets following high-dose intravenous administration of an adeno-associated virus vector expressing human SMN. *Hum. Gene Ther.* **29**, 285–298 (2018).
35. Angela, L. et al. Death after high-dose rAAV9 gene therapy in a patient with Duchenne's muscular dystrophy. *N. Engl. J. Med.* **389**, 1203–1210 (2023).
36. Das, R. et al. Lipid nanoparticle–mRNA engineered dendritic cell based adoptive cell therapy enhances cancer immune response. *Small Methods* **9**, 2400633 (2025).
37. Reinhardt, R. L., Hong, S., Kang, S.-J., Wang, Z. & Locksley, R. M. Visualization of IL-12/23p40 in vivo reveals immunostimulatory dendritic cell migrants that promote Th1 differentiation. *J. Immunol.* **177**, 1618–1627 (2006).
38. Belderbos, M. E. et al. Neonatal plasma polarizes TLR4-mediated cytokine responses towards low IL-12p70 and high IL-10 production via distinct factors. *PLoS ONE* **7**, e33419 (2012).
39. Brombacher, F., Kastelein, R. A. & Alber, G. Novel IL-12 family members shed light on the orchestration of Th1 responses. *Trends Immunol.* **24**, 207–212 (2003).
40. Spadaro, F. et al. IFN-α enhances cross-presentation in human dendritic cells by modulating antigen survival, endocytic routing, and processing. *Blood* **119**, 1407–1417 (2012).
41. Murphy, T. L. et al. Transcriptional control of dendritic cell development. *Annu. Rev. Immunol.* **34**, 93–119 (2016).
42. Tussiwand, R. et al. Compensatory dendritic cell development mediated by BATF–IRF interactions. *Nature* **490**, 502–507 (2012).
43. Liang, Y., Hannan, R. & Fu, Y.-X. Type I IFN activating type I dendritic cells for antitumor immunity. *Clin. Cancer Res.* **27**, 3818–3824 (2021).
44. Hildner, K. et al. Batf3 deficiency reveals a critical role for CD8α+ dendritic cells in cytotoxic T cell immunity. *Science* **322**, 1097–1100 (2008).
45. Liu, Y., Beyer, A. & Aebersold, R. On the dependency of cellular protein levels on mRNA abundance. *Cell* **165**, 535–550 (2016).
46. Nutt, S. L. & Chopin, M. Transcriptional networks driving dendritic cell differentiation and function. *Immunity* **52**, 942–956 (2020).
47. Chopin, M. et al. Transcription factor PU.1 promotes conventional dendritic cell identity and function via induction of transcriptional regulator DC-SCRIPT. *Immunity* **50**, 77–90.e5 (2019).
48. Kelly, A. & Trowsdale, J. Genetics of antigen processing and presentation. *Immunogenetics* **71**, 161–170 (2019).
49. Honda, K., Takaoka, A. & Taniguchi, T. Type I inteferon gene induction by the interferon regulatory factor family of transcription factors. *Immunity* **25**, 349–360 (2006).
50. Abbas, A. et al. The activation trajectory of plasmacytoid dendritic cells in vivo during a viral infection. *Nat. Immunol.* **21**, 983–997 (2020).
51. Sabado, R. L., Balan, S. & Bhardwaj, N. Dendritic cell-based immunotherapy. *Cell Res.* **27**, 74–95 (2017).
52. Perez, C. R. & De Palma, M. Engineering dendritic cell vaccines to improve cancer immunotherapy. *Nat. Commun.* **10**, 5408 (2019).
53. Kauffman, K. J. et al. Optimization of lipid nanoparticle formulations for mRNA delivery in vivo with fractional factorial and definitive screening designs. *Nano Lett.* **15**, 7300–7306 (2015).
54. Oberli, M. A. et al. Lipid nanoparticle assisted mRNA delivery for potent cancer immunotherapy. *Nano Lett.* **17**, 1326–1335 (2017).
55. Simmons, D. P. et al. Type I IFN drives a distinctive dendritic cell maturation phenotype that allows continued class II MHC synthesis and antigen processing. *J. Immunol.* **188**, 3116–3126 (2012).
56. Duan, Z. & Luo, Y. Targeting macrophages in cancer immunotherapy. *Signal Transduct. Target. Ther.* **6**, 127 (2021).
57. Kim, J. et al. Albumin turnover: FcRn-mediated recycling saves as much albumin from degradation as the liver produces. *Am. J. Physiol. Gastrointest. Liver Physiol.* **290**, G352–G360 (2006).
58. Waldmann, T. A. et al. Safety (toxicity), pharmacokinetics, immunogenicity, and impact on elements of the normal immune system of recombinant human IL-15 in rhesus macaques. *Blood* **117**, 4787–4795 (2011).
59. Conlon, K. C., Miljkovic, M. D. & Waldmann, T. A. Cytokines in the treatment of cancer. *J. Interferon Cytokine Res.* **39**, 6–21 (2018).
60. Jia, Z. et al. IL12 immune therapy clinical trial review: novel strategies for avoiding CRS-associated cytokines. *Front. Immunol.* **13**, 952231 (2022).
61. Xue, D., Hsu, E., Fu, Y.-X. & Peng, H. Next-generation cytokines for cancer immunotherapy. *Antib. Ther.* **4**, 123–133 (2021).
62. Domingos-Pereira, S. et al. Tumor-microenvironment characterization of the MB49 non-muscle-invasive bladder-cancer orthotopic model towards new therapeutic strategies. *Int. J. Mol. Sci.* **24**, 123 (2023).
63. Bruni, E. et al. Intrahepatic $CD69^{+}V\delta1$ T cells re-circulate in the blood of patients with metastatic colorectal cancer and limit tumor progression. *J. Immunother. Cancer* **10**, e004579 (2022).
64. Sancho, D., Gómez, M. & Sánchez-Madrid, F. CD69 is an immunoregulatory molecule induced following activation. *Trends Immunol.* **26**, 136–140 (2005).
65. Baharom, F. et al. Systemic vaccination induces $CD8^{+}$ T cells and remodels the tumor microenvironment. *Cell* **185**, 4317–4332 (2022).
66. Kranz, L. M. et al. Systemic RNA delivery to dendritic cells exploits antiviral defence for cancer immunotherapy. *Nature* **534**, 396–401 (2016).
67. Marabelle, A., Kohrt, H., Caux, C. & Levy, R. Intratumoral immunization: a new paradigm for cancer therapy. *Clin. Cancer Res.* **20**, 1747–1756 (2014).
68. Aznar, M. A. et al. Intratumoral delivery of immunotherapy—act locally, think globally. *J. Immunol.* **198**, 31–39 (2017).
69. Ferris, S. T. et al. cDC1 vaccines drive tumor rejection by direct presentation independently of host cDC1. *Cancer Immunol. Res.* **10**, 920–931 (2022).
70. Freeman, G. J. et al. Engagement of the PD-1 immunoinhibitory receptor by a novel B7 family member leads to negative regulation of lymphocyte activation. *J. Exp. Med.* **192**, 1027–1034 (2000).
71. Van der Jeught, K. et al. Dendritic cell targeting mRNA lipopolyplexes combine strong antitumor T-cell immunity with improved inflammatory safety. *ACS Nano* **12**, 9815–9829 (2018).
72. Rudra, A. et al. Degradable cyclic amino alcohol ionizable lipids as vectors for potent influenza mRNA vaccines. *Nat. Nanotechnol.* **20**, 1831–1842 (2025).
73. Li, X., Syrovets, T., Paskas, S., Laumonnier, Y. & Simmet, T. Mature dendritic cells express functional thrombin receptors triggering chemotaxis and CCL18/pulmonary and activation-regulated chemokine induction. *J. Immunol.* **181**, 1215–1223 (2008).
74. Albert, M. L. et al. Immature dendritic cells phagocytose apoptotic cells via αvβ5 and CD36, and cross-present antigens to cytotoxic T lymphocytes. *J. Exp. Med.* **188**, 1359–1368 (1998).
75. Deng, Z. J., Liang, M., Monteiro, M., Toth, I. & Minchin, R. F. Nanoparticle-induced unfolding of fibrinogen promotes Mac-1 receptor activation and inflammation. *Nat. Nanotechnol.* **6**, 39–44 (2011).

76. Cheng, C. et al. Recognition of lipoproteins by scavenger receptor class A members. *J. Biol. Chem.* **297**, 100948 (2021).
77. Qu, J. et al. Low-density lipoprotein receptor-related protein 1 (LRP1) is a novel receptor for apolipoprotein A4 (APOA4) in adipose tissue. *Sci. Rep.* **11**, 13289 (2021).
78. Jayaraman, M. et al. Maximizing the potency of siRNA lipid nanoparticles for hepatic gene silencing in vivo. *Angew. Chem. Int. Ed. Engl.* **51**, 8529–8533 (2012).
79. Gupta, A., Andresen, J. L., Manan, R. S. & Langer, R. Nucleic acid delivery for therapeutic applications. *Adv. Drug Deliv. Rev.* **178**, 113834 (2021).
80. Li, C. et al. Mechanisms of innate and adaptive immunity to the Pfizer-BioNTech BNT162b2 vaccine. *Nat. Immunol.* **23**, 543–555 (2022).
81. Yu, H., Lin, L., Zhang, Z., Zhang, H. & Hu, H. Targeting NF-κB pathway for the therapy of diseases: mechanism and clinical study. *Signal Transduct. Target. Ther.* **5**, 209 (2020).

Methods

Animal studies

All animal studies were approved by the Massachusetts Institute of Technology and Massachusetts General Hospital Institutional Animal Care and Use Committee (animal protocol no. 2021N000272) and were consistent with local, state and federal regulations as applicable. Animals were housed in a pathogen-free environment at 70 °F and 40% humidity with a 12-h day–night cycle with access to food and water ad libitum. All mice were 6–8 weeks old at the start of experiments and were sourced from Jackson Labs. C56Bl/6J mice were used for all tumor experiments (except B16-F10 metastatic tumors) and for HA vaccination experiments. B6.129-*Il12b*$^{tm1.1Lky}$/J mice were used for IL-12 eYFP reporter assays. B6(Cg)-*Tyr*$^{c-2J}$/J mice were used for B16-F10 metastatic experiments. BALB/cJ mice were used for SARS-CoV-2 vaccination experiments.

In vivo imaging system (IVIS) Imaging

For bioluminescence imaging, D-luciferin potassium salt (Revvity) in PBS was injected intraperitoneally at a dose of 200 mg kg^{-1}. Then, 15 min after injection, mice were anesthetized with isoflurane for live imaging or killed for organ collection and ex vivo imaging.

LNP formulation

LNPs were formulated as described previously[72]. DOPE (Avanti), cholesterol (Millipore-Sigma) and DMG-PEG2k (Avanti) stocks were prepared by dissolving at 10 mg ml^{-1} in ethanol. Ionizable lipids (Supplementary Methods) were dissolved at 40 mg ml^{-1} in ethanol. The lipid phases were prepared using a previously reported formulation summarized in Supplementary Table 1. Separately, the aqueous phases for formulations were made by preparing a 133 ng µl^{-1} solution of mRNA in 10 mM citrate pH 3.0. The LNPs were then formulated using a herringbone microfluidic mixing channel, mixing the aqueous and lipid phases in a 3:1 volume ratio at a total flow rate of 1.2 ml min^{-1}.

Following formulation, LNPs were exchanged into PBS using Amicon centrifugal filters (100-kDa cutoff; Millipore-Sigma). Briefly, LNPs were diluted at least 4× with PBS and then concentrated, repeating three times before concentrating to the final desired volume such that the final pH was 7–7.5.

In cases where multiple mRNAs were delivered simultaneously (antigen + IR-mRNA), each mRNA-LNP was formulated separately, then mixed and coinjected. Doses were kept constant across all treatment conditions and each mRNA was mixed in equal proportions (for example, antigen alone: 10 µg; antigen + second RNA: 5 µg + 5 µg).

LNP characterization

LNP characterization was performed as described previously[72]. mRNA concentration and encapsulation were determined using a Quant-IT Ribogreen assay. LNPs were diluted in either native TE buffer (Thermo Fisher) or denaturing TE buffer + 0.5% Triton X-100 (Millipore-Sigma) to measure free and total mRNA, respectively. First, 50 µl of these unknowns were added to a black 96-well plate. Separately, standard curves ranging from 2 ng µl^{-1} to 0 ng µl^{-1} were prepared in each of these buffers and 50 µl of the unknowns were added to the same 96-well plate. Next, Quant-IT Ribogreen reagent (Thermo Fisher) was diluted 1:200 in TE buffer, and 100 µL of this solution was added to each of the wells. The well plate was then mixed at 400 rpm with a plate shaker for 5 min and the fluorescence was read with excitation at 485 nm and emission at 535 nm. LNPs were measured in triplicate and standards were measured in duplicate. RNA concentration in each of the unknown wells was calculated by fitting the standard curves with a linear trendline. Encapsulation efficiency (%EE) was calculated as follows:

$$\%\mathrm{EE} = \frac{(\text{total RNA}) - (\text{free RNA})}{\text{total RNA}} \times 100 \quad (1)$$

All dosing was performed on the basis of the total RNA concentration. Representative LNP characterization data are shown in Supplementary Table 2.

RNA synthesis

Hemagglutinin (A/Tasmania/503/2020) RNA was generously provided by Sanofi.

The mouse and human NIK and IRF8 and the SARS-CoV-2 spike (B.1.617.2) sequences were obtained by PCR from sequence optimized constructs in plasmids (GeneWiz). Sequences were codon-optimized using the open-source mRNAid tool[82]. The tdTomato open reading frame (ORF) was obtained from Addgene (plasmid 54642) using PCR. The FLuc ORF was obtained from pGL3 (Promega) using PCR. These ORFs were cloned into a custom mRNA plasmid containing a T7 promoter with a CleanCap AG site, 5′/3′ untranslated regions and a 100-nt poly(A) tail. Plasmids were transformed into NEB 5-alpha FIq *Escherichia coli* (New England Biolabs) according to the manufacturer's instructions. Plasmids were purified using mini or midi preps (Qiagen) according to the manufacturer's instructions. Sequences were verified using nanopore sequencing. Plasmids were then linearized using 10 U of NsiI-HF (New England Biolabs) per 1 µg of DNA in rCutSmart buffer (New England Biolabs) for 1 h at 37 °C. In vitro transcription (IVT) was then performed using the HiScribe T7 kit (New England Biolabs) according to the manufacturer's instructions for synthesis of CleanCap mRNA and N^1-methylpseudouridine triphosphate (TriLink) was substituted for UTP in all reactions to produce fully modified mRNA. Following IVT, template DNA was removed by adding 4 U of DNAse I (New England Biolabs) per 1 µg of template to the IVT reaction and incubating at 37 °C for 15 min. The mRNA was then purified using the Monarch RNA cleanup kit (500 µg) (New England Biolabs). The molecular weight of the RNA was verified using a Fragment Analyzer (Agilent). Representative results are shown in Supplementary Fig. 23.

Immunization studies

LNPs were formulated as described above with HA (A/Tasmania/503/2020), FLuc, NIK or IRF8 mRNA. All vaccination doses were normalized to a total mRNA dose of 1 µg; in cases where HA was mixed with another mRNA, the two mRNAs were mixed 50:50 w/w (0.5 µg of HA mRNA-LNPs + 0.5 µg of FLuc, NIK or IRF8 mRNA-LNPs). All LNPs were injected intramuscularly in the quadricep with an injection volume of 50 µl. All vaccination experiments followed a prime–boost dosing regimen with doses given on day 0 and day 21. On day 35, mice were killed, blood was collected by cardiac puncture and spleens were collected for further characterization.

Cell culture

B16-F10 and B16-F10-Luc2 were purchased from the American Type Culture Collection (ATCC). B16-OVA, MC38 and MB49 were purchased from Millipore-Sigma. These cells were routinely screened for murine pathogens and *Mycoplasma* contamination. Cells were cultured in DMEM supplemented with 4.5 g l^{-1} D-glucose, GlutaMAX and 10% FBS (Thermo Fisher).

BMDCs were cultured by isolating bone marrow from the femur and tibia of mice. Bone marrow cells were then resuspended at 1.5×10^6 cells ml^{-1} in RPMI 1640 supplemented with GlutaMAX (Thermo Fisher), 10% FBS (Thermo Fisher), 100 U per ml penicillin (Thermo Fisher), 100 µg ml^{-1} streptomycin (Thermo Fisher), 50 µM β-mercaptoethanol (Millipore), 200 ng ml^{-1} Flt3L-Fc (R&D Systems) and 20 ng ml^{-1} GM-CSF (R&D Systems). On day 9, nonadherent cells were harvested and used immediately.

IFN-I ELISAs

IFNα and IFNβ were measured in serum and the BMDC cell culture supernatant using ELISA kits (Biolegend) according to the manufacturer's instructions.

Binding antibody ELISAs

Clear, flat-bottomed, high-binding 96-well plates were coated with either spike (B.1.617.2) (Bio-Techne) or hemagglutinin (provided as a gift from Sanofi). Plates were coated overnight at 4 °C by adding 100 µl of a 1 µg ml^{-1} antigen solution in 100 mM carbonate buffer pH 9.6 to each well. The coated plates were then washed with ELISA wash buffer (Biolegend) and blocked for 1 h at room temperature with 150 µl of 1% BSA in PBS (Miltenyi Biotec). The plate was then washed again and 100 µl of serially diluted serum samples were then added to the plate and incubated at room temperature for 1 h. Next, the plate was washed and the secondary goat anti-mouse IgG, horseradish peroxidase (HRP)-conjugated antibody (Thermo Fisher) was diluted 1:3,000. Then, 100 µl of this solution was added to each well and incubated at room temperature for 1 h. After incubation, the plate was washed and 100 µl of TMB chromogen solution (Thermo Fisher) was added to each well and incubated for 30 min. Finally, the HRP reaction was stopped by the addition of 100 µl of 0.5 M H_2SO_4. The absorbance of each well was immediately read at 450 nm with 600 nm as a reference using an Infinite M200 Pro (Tecan) plate reader. The resultant data were then fitted with a four-parameter logistic sigmoidal curve and the endpoint titers were taken as the points at which the curve crossed four times the absorbance of the blank wells.

IFNγ ELISpot

Spleens were dissociated into single-cell suspensions by mashing through a 70-µm strainer (Corning). Cells were pelleted and red blood cells (RBCs) were lysed using RBC lysis buffer (Biolegend) for 5 min on ice. The RBC lysis reaction was stopped by adding four volumes of PBS + 1% BSA. Cells were then pelleted, resuspended in PBS + 1% BSA and counted using a Countess 3 automated cell counter (Thermo Fisher).

Mouse IFN-γ ELISpots (BD Biosciences) were performed according to the manufacturer's instructions. Briefly, ELISpot plates were coated with the capture antibody overnight at 4 °C, washed and then blocked for 2 h at room temperature using complete medium: 10% FBS (Thermo Fisher) in RPMI 1640 + GlutaMAX (Thermo Fisher). After blocking, splenocytes were plated at the indicated density in 100 µl of complete medium. Separately, hemagglutinin (A/Tasmania/503/2020) peptide pools restricted by MHC-I and MHC-II were obtained as gifts from Sanofi and were dissolved in DMSO at 0.2 mg ml^{-1}. These peptide pools were diluted 1:100 in complete medium and 100 µl of this solution was added to the cells in the ELISpot plate (final peptide concentration: 1 µg ml^{-1}). Cells were stimulated for 16 h. The supernatant was then collected for further analysis and spots were developed on the plate according to the manufacturer's instructions. Plates were allowed to dry overnight and then imaged on an ImmunoSpot Analyzer (C.T.L.).

Flow cytometry

Lymph nodes, tumors and spleens were dissociated by using micro tissue homogenizers (Kimble Biomasher II). Tumors were digested by the addition of collagenase IV at 0.2 mg ml^{-1} in RPMI 1640 followed by vigorous shaking at 37 °C for 45 min. The digested tumor tissues, lymph node and spleen were filtered through a 70-µm cell strainer and resuspended in protein-free PBS. For the spleen, red blood cells (RBCs) were lysed with RBC lysis solution (Biolegend). Following dissociation, cells were stained for 30 min at 4 °C with AquaAmine live/dead fixable viability stain (Thermo Fisher), then Fc blocked (Miltenyi) and stained with the antibodies of interest at 4 °C for 30 min. Following staining, cells were washed twice and then fixed with 4.2% PFA (BD Biosciences) at 4 °C for 15 mins. Lastly, cells were stored in PBS + 1% BSA (Miltenyi) before analysis and analyzed within 2 days on an Attune NxT flow cytometer (Invitrogen) and BD FACS Symphony A3 (BD Biosciences). Compensation was performed using UltraComp eBeads compensation beads (Thermo Fisher). Data were analyzed using FlowJo version 10. Representative gating for flow cytometry studies is shown in Supplementary Figs. 24–29. The list of antibodies is shown in Supplementary Table 3.

Ai14 reporter mice transfection analysis

Ai14D mice were IV injected with AMG514 and cKK-E12 LNPs encapsulating Cre recombinase mRNA (0.25 mg kg^{-1} per mouse; TriLink). At 72 h after injection, spleen and liver tissues were isolated and digested by the addition of collagenase IV at 0.2 mg ml^{-1} in RPMI 1640, followed by vigorous shaking at 37 °C for 45 min. The digested tissues were passed through a 70-µm cell strainer and the cell suspensions were centrifuged and resuspended in staining buffer. Cells were incubated with antibodies against lineage-specific markers in staining buffer for 30 min at 4 °C, followed by flow cytometric analysis as described above.

Histology

Tissues were isolated and fixed for 24 h in 10% neutral buffered formalin at 4 °C. After fixing, tissues were washed with deionized water and stored in 70% ethanol. Tissues were then cut in the transverse direction along their midplane, dehydrated and paraffin-embedded. Next, 4-µm-thick sections were mounted on slides and deparaffinized. These were then either subjected to hematoxylin and eosin (H&E) staining or further processing for IHC.

For IHC, the deparaffinized tissues were subjected to heat-mediated antigen retrieval in pH 6 citrate buffer at 97 °C for 20 min. Sections then underwent endogenous peroxidase deactivation for 10 min, followed by blocking for 30 min. After blocking, the primary antibody was added for 60 min, the slides were washed and the secondary antibody was added for 30 min. After washing, staining was performed with DAB substrate for 5 min, followed by counterstaining with hematoxylin. Slides were then mounted and scanned using a slide scanner with a ×40 objective.

Tumor inoculation and tumor therapy

Tumor cell lines were detached from culture flasks and resuspended in PBS at an appropriate concentration for tumor inoculation. Subcutaneous tumors were inoculated by injecting cells into the flank of mice. Metastatic tumors were inoculated by IV tail-vein injection. Subcutaneous tumor volumes were measured by caliper and their volumes calculated according to the formula $V = 0.5 \times L \times W^2$.

Luminex

Multiplexing analysis was performed using the Luminex 200 system (Luminex, Eve Technologies). All samples were diluted 1:1 with PBS + 1% BSA (Miltenyi Biotec). Samples were analyzed using the Eve Technologies mouse high sensitivity 18-plex discovery assay (Millipore-Sigma) according to the manufacturer's protocol. The 18-plex assay consisted of GM-CSF, IFNγ, IL-1, IL-2, IL-4, IL-5, IL-6, IL-7, IL-10, IL-12(p70), IL-13, IL-17A, KC/CXCL1, LIX, MCP1, MIP-2 and TNF. Assay sensitivities of these markers range from 0.06–9.06 pg ml^{-1} for the 18-plex. Serum collected 6 h after vaccination was analyzed using the Eve Technologies mouse-focused 10-plex discovery assay (Millipore-Sigma) according to the manufacturer's protocol. The 10-plex assay consisted of GM-CSF, IFNγ, IL-1, IL-2, IL-4, IL-6, IL-10, IL-12p70, MCP1 and TNF. Sensitivities of these markers ranged from 0.4 to 10.9 pg ml^{-1} for the 10-plex assay. Individual analyte sensitivity values are available in the Millipore-Sigma MILLIPLEX MAP protocol.

RNA-seq

Additional methods for scRNA-seq are provided in the Supplementary Methods.

Human DC differentiation from human primary bone marrow CD34$^+$ cells

Human DCs were differentiated from human primary bone marrow CD34$^+$ cell using a mouse OP9 coculture method as reported

in previously established protocols[83]. The mouse OP9 cell line (ATCC, CRL-2749) was cultured in T75 flasks in OP9 medium (αMEM, 20% FCS and penicillin–streptomycin) at 37 °C and 5% CO_2 and maintained at a density of 4×10^3–1×10^4 cells per cm^2 with medium changes every 3–4 days. For plating, OP9 cells were seeded into 96-well U-bottom plates at 5,000 cells per well. Human primary bone marrow $CD34^+$ cells (ATCC PCS-800-012) were resuspended at 1.5×10^4 cells per ml in DC differentiation medium (αMEM supplemented with 10% FCS, 1% penicillin–streptomycin, 100 ng ml^{-1} Flt3L, 20 ng ml^{-1} stem cell factor and 20 ng ml^{-1} GM-CSF). OP9 medium was gently removed and replaced with 200 µl of $CD34^+$ cell suspension (3,000 cells per well). Cultures were maintained with half-medium changes on day 6 and subsequently on days 12 and 18. Differentiated cells were harvested on day 19 by gentle pipetting, filtered through 50-µm strainers and resuspended in appropriate buffers for flow cytometric analysis. Immature human DCs were treated with human NIK, IRF8 and FLuc (control) mRNAs on day 6, 12 and 18, followed by analysis on day 19.

Statistical analysis

Statistical analysis was performed using GraphPad Prism.

Reporting summary

Further information on research design is available in the Nature Portfolio Reporting Summary linked to this article.

Data availability

All data that support the findings of this study are provided within the manuscript and its Supplementary Information. The scRNA-seq data were deposited to the National Center for Biotechnology Information Gene Expression Omnibus under accession number (GSE325843). Source data are provided with this paper.

References

82. Vostrosablin, N. et al. mRNAid, an open-source platform for therapeutic mRNA design and optimization strategies. *NAR Genom. Bioinform.* **6**, lqae028 (2024).
83. Lutz, M. B. et al. Guidelines for mouse and human DC generation. *Eur. J. Immunol.* **53**, 2249816 (2023).

Acknowledgements

This work was supported by Sanofi (formerly Translate Bio) to D.G.A., the National Institutes of Health (R61AI161805 to D.G.A.) and the Marble Center for Cancer Nanomedicine (to D.G.A. and R.L.). This work was also supported in part by the Koch Institute Support (core) grant 5P30-CA014051 from the National Cancer Institute. We thank the Koch Institute's Robert A. Swanson (1969) Biotechnology Center for technical support, specifically the Flow Cytometry Core, the Hope Babette Tang (1983) Histology Core, the BioMicro Center, the Animal Imaging and Preclinical Testing Core and the Biopolymers and Proteomics Core. R.D. was supported by the National Cancer Institute (T32 CA079443). Research leading up to IRF8 and NIK discovery was supported by the CSB discovery fund, the Karin Grunebaum Cancer Research Foundation and the Department of Defense (HT9425-24-1-0424) (to C.G.). R.W. was supported by the National Institutes of Health (5R01CA257623, R33CA277820 and R01CA281735).

Author contributions

A.G., R.D., K.R., T.J., Q.T.C.N., X.G., S.T., A.R. and C.G. performed the experiments and analyzed the data. A.G., R.D., K.R., R.W., C.G. and D.G.A. discussed the results and wrote the paper with input from all authors. R.L., C.G., R.W. and D.G.A. acquired funding and supervised the project. A.G., R.D. and K.R. contributed equally and all reserve the right to list themselves first on their curricula vitae.

Competing interests

D.G.A. has advised Alnylam, Sanofi, Translate Bio, oRNA Therapeutics and Combined Therapeutics. R.L. has advised Alnylam, Moderna and Combined Therapeutics. A list of entities with which R.L. is involved, compensated or uncompensated, is available online (www.dropbox.com/s/yc3xqb5s8s94v7x/Rev%20Langer%20COI.pdf?dl=0). Patent applications covering aspects of this work have been filed by D.G.A., A.G., K.R., R.D., R.W. and C.G. The other authors declare no competing interests.

Additional information

Extended data is available for this paper at https://doi.org/10.1038/s41587-026-03115-2.

Supplementary information The online version contains supplementary material available at https://doi.org/10.1038/s41587-026-03115-2.

Correspondence and requests for materials should be addressed to C. Garris or D. G. Anderson.

Peer review information *Nature Biotechnology* thanks Carlos-Filipe Pereira and the other, anonymous, reviewer(s) for their contribution to the peer review of this work.

https://doi.org/10.1038/s41587-026-03115-2

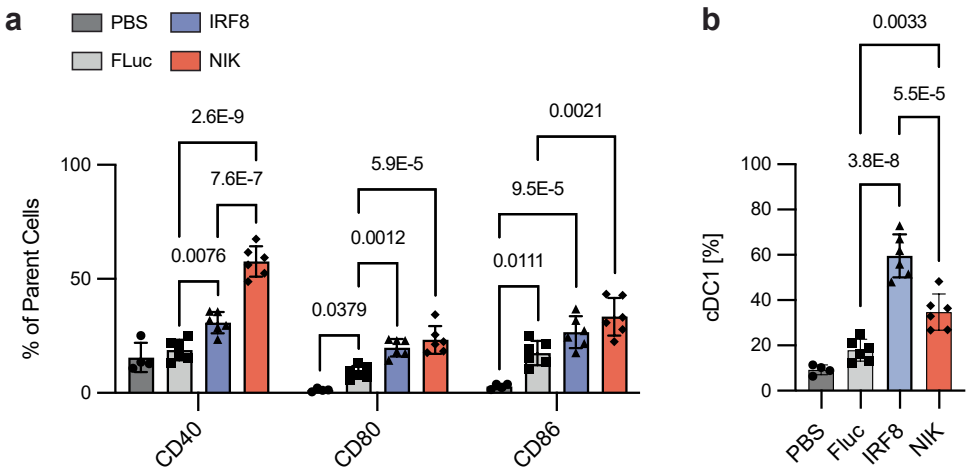

Extended Data Fig. 1 | Human NIK and IRF8 mRNA treatment induces maturation of human DCs. a Flow cytometry quantification of maturation markers in human DCs following treatment with 50 ng of mRNA. Mean ± S.D. shown, n = 4 wells for PBS and 6 wells for others. **b** percentage cDC1 cells after IR-mRNA treatment. Mean ± S.D. shown, n = 4 wells for PBS and 6 wells for others. Statistical significance was analyzed using a one-way analysis of variance with a two-tailed Tukey's multiple comparisons test with a single pooled variance.

https://doi.org/10.1038/s41587-026-03115-2

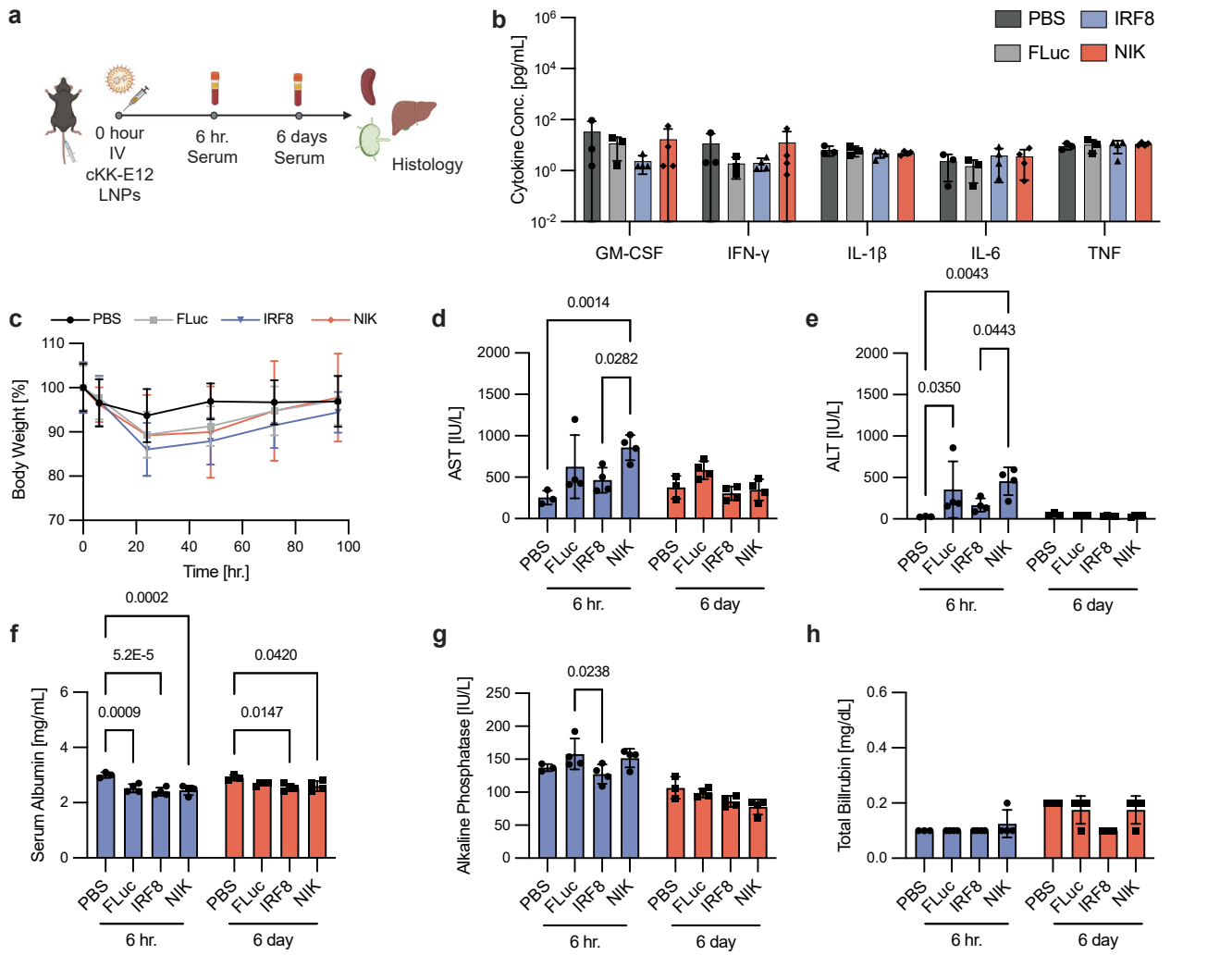

Extended Data Fig. 2 | Additional tolerability evaluation data. a Schematic illustrating the treatment of C57BL/6 J mice with cKK-E12 mRNA-LNPs, followed by blood and organ collection at 6 hours and 6 days post-injection. **b** Comparison of IL-1ß, IL-6, TNF, GM-CSF, and IFN-γ levels in serum at 6 hour and day 6 post injection. Mean ± S.D. shown, n = 3 mice for PBS and 4 mice for others. **c** Body weight measurement of the treated mice monitored up to 4 days. Mean ± S.D. shown, n = 3 mice for PBS and 4 mice for all others. **d-h** Graphs showing comparison of AST (**d**), ALT (**e**), serum albumin (**f**), alkaline phosphatase (**g**), and total bilirubin (**h**) levels in serum at 6 hr. and 6 days post injection. Mean ± S.D. shown. n = 3 mice for PBS and 4 mice for others. Statistical significance was analyzed using a repeated measures two-way analysis of variance with a two-tailed Tukey's multiple comparisons test using a single pooled variance (**d**–**e**). Panel **a** created in BioRender; Gupta, A. https://biorender.com/itm02de (2026).

https://doi.org/10.1038/s41587-026-03115-2

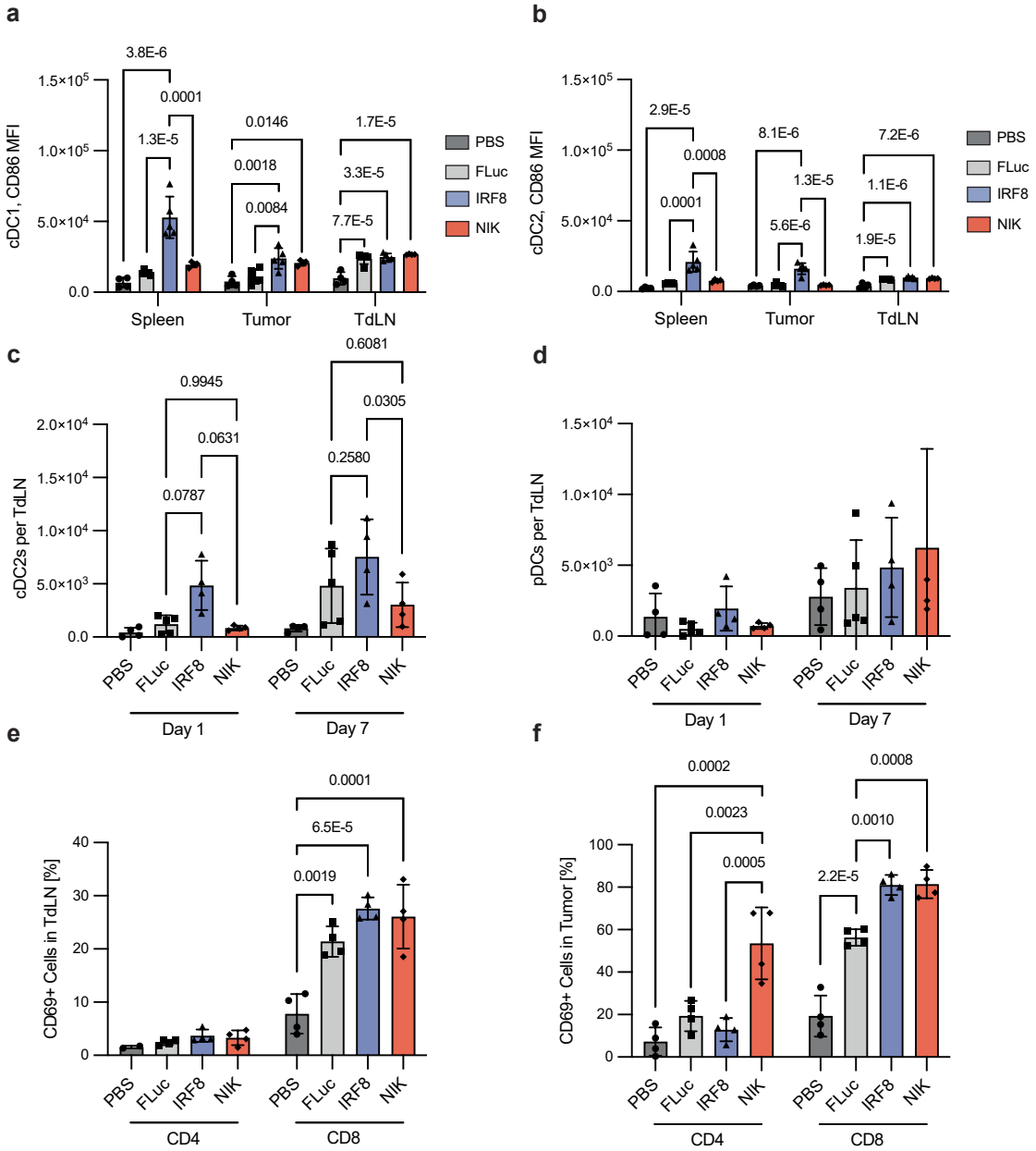

Extended Data Fig. 3 | Additional tumor immune phenotyping characterization. a,b Graphs showing CD86 MFI in cDC1 (**a**) and cDC2 (**b**) in TdLN, spleen, and tumor on day 1 after IR-mRNA treatment. Mean ± S.D. shown, n = 4 mice for PBS/FLuc and 5 mice for IRF8/NIK. **c,d** cDC2 (**c**), pDC (**d**) counts in the TdLN in day 1 and day 7. Mean ± S.D. shown, n = 4 mice for PBS/FLuc and 5 mice for IRF8/NIK. **e,f** Quantitative results of CD69 activated CD4+ and CD8 + T cells in tumor draining lymph nodes (**e**), and tumors (**f**) 7 days post treatment with mRNA-LNPs. Mean ± S.D. shown, n = 4 mice for PBS/FLuc and 5 mice for IRF8/NIK. Statistical analysis was performed using a one-way analysis of variance with Tukey's multiple comparisons test with a single pooled variance (**a,b,e,f**), a repeated measurements two-way analysis of variance with a two-tailed Tukey's multiple comparisons test using a single pooled variance (**c,d**).

https://doi.org/10.1038/s41587-026-03115-2

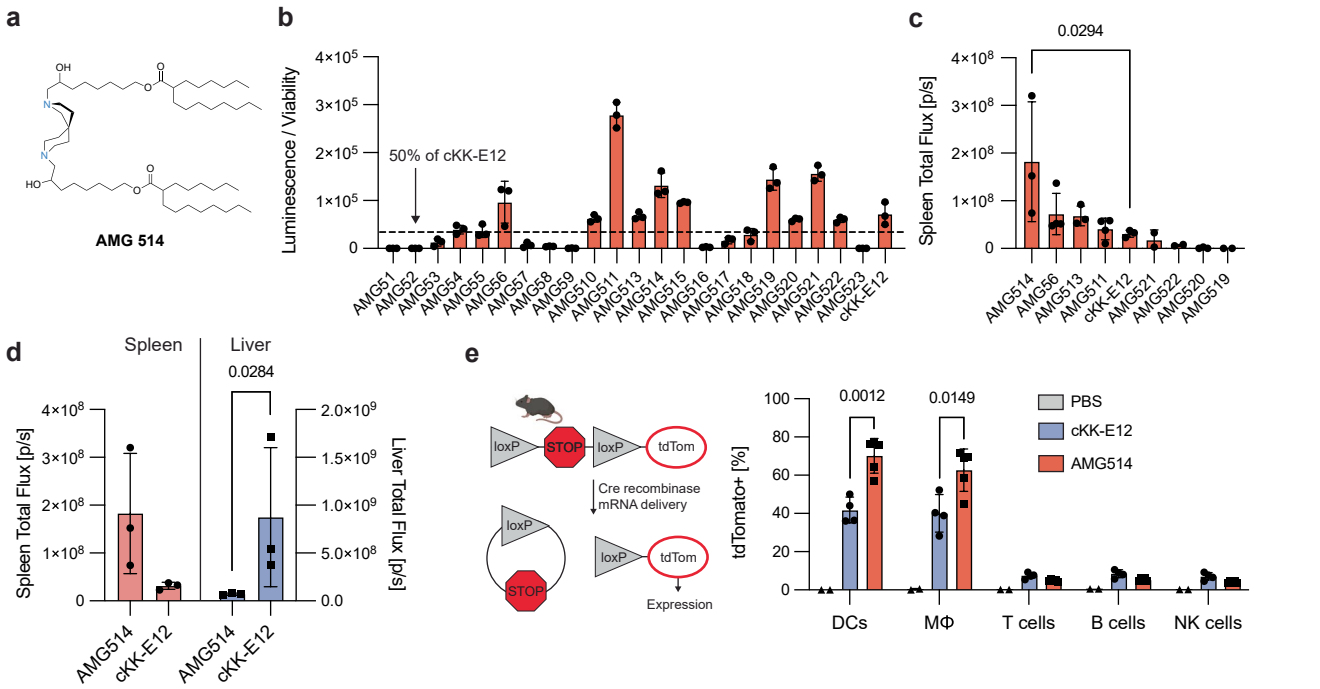

Extended Data Fig. 4 | Spirocyclic di-amine ionizable lipid exhibit improved delivery to splenic APCs. a Molecular structure of top-performing ionizable lipid AMG514. **b** In vitro transfection data for AMG lipids in DC2.4 cells after treatment with FLuc encapsulating LNPs dosed at 40 ng/well, shown in bar graph format. Mean ± s.d., n = 3 wells per group. **c** Quantification of FLuc protein expression in spleen following IV injection of Top 8 ionizable lipids. Mean ± S.D. shown, n = 3 mice. **d** Liver and spleen expression for AMG514 and cKK-E12 (FLuc mRNA, dose = 1 µg, t = 6 hours). Mean ± S.D. shown, n = 3 mice. **e** Schematic of the Ai14/Cre mRNA mouse model (left), and flow cytometry quantification of tdTomato expressing cells in spleen, 48 hours after intravenous injection of Cre mRNA encapsulated in cKK-E12 and AMG514 (right, dose = 5 µg). Mean ± S.D. shown, n = 4–5 mice. Statistical significance was analyzed using a one-way analysis of variance with a two-tailed Tukey's multiple comparisons test using a single pooled variance (**c**), a two-way analysis of variance with a two-tailed Fisher's least squared differences test using a single pooled variance (**d**), or an unpaired two-tailed t-test (**e**). MΦ – Macrophage; RLU, relative luminescence unit. Panel **e** created in BioRender; Reed, K. https://biorender.com/rv73rc7 (2026).

https://doi.org/10.1038/s41587-026-03115-2

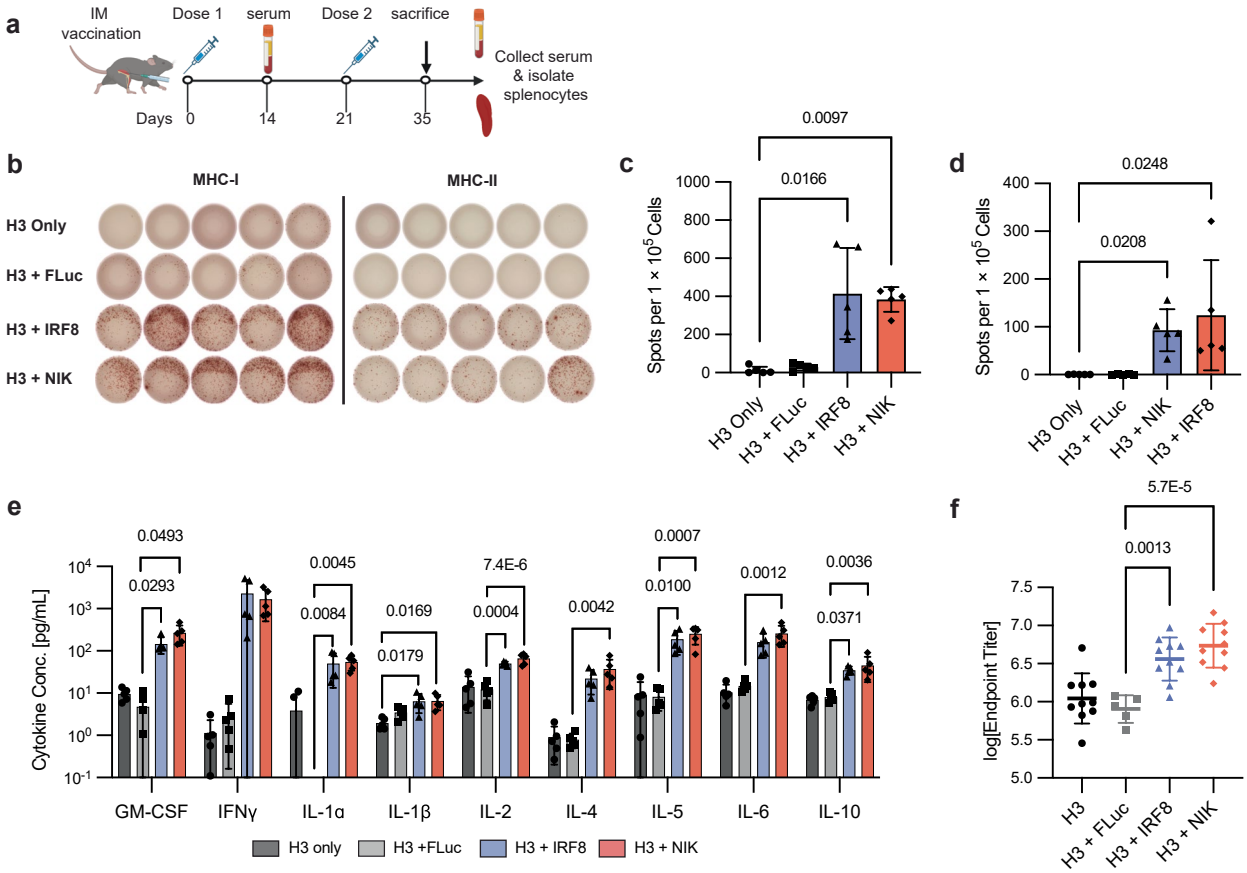

Extended Data Fig. 5 | IR-mRNAs boost the adaptive immune response for influenza vaccines. a Vaccination protocol used for the vaccine experiments. C57Bl/6J mice were vaccinated on days 0 and 14 with either H3 HA mRNA alone (1 µg) or H3 HA mRNA combined with a second mRNA as indicated (0.5 µg + 0.5 µg). **b-d** Day 35 peptide pool stimulated splenocyte IFN-γ ELISPOT images (**b**), and quantified SFU for MHC-I (**c**) and MHC-II (**d**). Mean ± S.D. shown, n = 5 mice. **e** Cytokine levels in the cell culture supernatant of peptide-stimulated splenocytes from vaccinated mice following vaccination. Mean ± S.D. shown, n = 5 mice. **f** Day 35 HA binding antibody titers. Mean ± S.D. shown, n = 10 mice for H3, H3 + IRF8, and H3 + NIK, 5 for H3 + FLuc. Statistical significance was analyzed using a Kruskal-Wallis test with Dunn's multiple comparisons (**c,d**) or a one-way analysis of variance with Tukey's multiple comparisons (**e,f**). Panel **a** created in BioRender; Gupta, A. https://biorender.com/vbgjiwv (2026).

nature portfolio

Corresponding author(s): Daniel G. Anderson, Chris Garris

Last updated by author(s): Mar 27, 2026

Reporting Summary

Nature Portfolio wishes to improve the reproducibility of the work that we publish. This form provides structure for consistency and transparency in reporting. For further information on Nature Portfolio policies, see our Editorial Policies and the Editorial Policy Checklist.

Statistics

For all statistical analyses, confirm that the following items are present in the figure legend, table legend, main text, or Methods section.

n/a	Confirmed
☐	☒ The exact sample size (*n*) for each experimental group/condition, given as a discrete number and unit of measurement
☐	☒ A statement on whether measurements were taken from distinct samples or whether the same sample was measured repeatedly
☐	☒ The statistical test(s) used AND whether they are one- or two-sided *Only common tests should be described solely by name; describe more complex techniques in the Methods section.*
☐	☒ A description of all covariates tested
☐	☒ A description of any assumptions or corrections, such as tests of normality and adjustment for multiple comparisons
☐	☒ A full description of the statistical parameters including central tendency (e.g. means) or other basic estimates (e.g. regression coefficient) AND variation (e.g. standard deviation) or associated estimates of uncertainty (e.g. confidence intervals)
☐	☒ For null hypothesis testing, the test statistic (e.g. *F*, *t*, *r*) with confidence intervals, effect sizes, degrees of freedom and *P* value noted *Give P values as exact values whenever suitable.*
☒	☐ For Bayesian analysis, information on the choice of priors and Markov chain Monte Carlo settings
☒	☐ For hierarchical and complex designs, identification of the appropriate level for tests and full reporting of outcomes
☒	☐ Estimates of effect sizes (e.g. Cohen's *d*, Pearson's *r*), indicating how they were calculated

Our web collection on statistics for biologists contains articles on many of the points above.

Software and code

Policy information about availability of computer code

Data collection	In vivo data was collected using a xenogen in vivo imaging system. Flow cytometry was performed using Attune NxT Flow Cytometer (Invitrogen) and FACS Symphony A3 flow cytometer (BD Biosciences). Size was measured using a Malvern Zetasizer Dynamic Light Scattering instrument.
Data analysis	Data was analyzed using GraphPad Prism 10/11. Flow cytometry data was analyzed using Flowjo 10. scRNA-seq analysis was performed with R v4.5.2.

For manuscripts utilizing custom algorithms or software that are central to the research but not yet described in published literature, software must be made available to editors and reviewers. We strongly encourage code deposition in a community repository (e.g. GitHub). See the Nature Portfolio guidelines for submitting code & software for further information.

Data

Policy information about availability of data

All manuscripts must include a data availability statement. This statement should provide the following information, where applicable:

- Accession codes, unique identifiers, or web links for publicly available datasets
- A description of any restrictions on data availability
- For clinical datasets or third party data, please ensure that the statement adheres to our policy

All data that support the findings of this study are provided within the manuscript and its supplementary information. Source data are available for the Figures 1–7 and the Extended Figures 1–4 in the manuscript.

Research involving human participants, their data, or biological material

Policy information about studies with human participants or human data. See also policy information about sex, gender (identity/presentation), and sexual orientation and race, ethnicity and racism.

Reporting on sex and gender	N/A
Reporting on race, ethnicity, or other socially relevant groupings	N/A
Population characteristics	N/A
Recruitment	N/A
Ethics oversight	N/A

Note that full information on the approval of the study protocol must also be provided in the manuscript.

Field-specific reporting

Please select the one below that is the best fit for your research. If you are not sure, read the appropriate sections before making your selection.

☒ Life sciences ☐ Behavioural & social sciences ☐ Ecological, evolutionary & environmental sciences

For a reference copy of the document with all sections, see nature.com/documents/nr-reporting-summary-flat.pdf

Life sciences study design

All studies must disclose on these points even when the disclosure is negative.

Sample size	Sample sizes were determined based on our previous experience with in vivo LNP and cancer studies to balance statistical power with minimizing animal usage. For in vitro tested we selected n = 3-6 for most studies based on previous experience necessary to identify statistically significant differences between treatment groups. For in vivo immune testing, we selected n = 4-5 to achieve adequate statistical power to determine differences between treatment groups. For tumor survival studies we selected n = 5 - 16 based upon the tumor type in order to achieve statistically significant conclusions.
Data exclusions	No data were excluded from analysis.
Replication	Experiments were repeated 2-3 times to confirm reproducibility, specific sample sizes and details are indicated in the figure captions
Randomization	Animals and other experimental groups (such as animal tissues, in vitro wells) were randomly selected to be put in different groups.
Blinding	Due to the constraints of the small study team, experimental blinding was not feasible. To mitigate potential bias, all analysis was performed using standardized protocols and objective criteria.

Reporting for specific materials, systems and methods

We require information from authors about some types of materials, experimental systems and methods used in many studies. Here, indicate whether each material, system or method listed is relevant to your study. If you are not sure if a list item applies to your research, read the appropriate section before selecting a response.

Materials & experimental systems

n/a	Involved in the study
☐	☒ Antibodies
☐	☒ Eukaryotic cell lines
☒	☐ Palaeontology and archaeology
☐	☒ Animals and other organisms
☒	☐ Clinical data
☒	☐ Dual use research of concern
☒	☐ Plants

Methods

n/a	Involved in the study
☒	☐ ChIP-seq
☐	☒ Flow cytometry
☒	☐ MRI-based neuroimaging

Antibodies

Antibodies used	All antibodies are listed in Supplemental Table 3.
Validation	All antibodies were validated by the manufacturers and these clones have been used extensively for flow cytometry.

Eukaryotic cell lines

Policy information about cell lines and Sex and Gender in Research

Cell line source(s)	B16-F10, B16-F10-Luc2, OP9, and primary human CD34+ cells were purchased from ATCC. B16-OVA, MC38, and MB49 were purchased from Millipore-Sigma.
Authentication	Cell lines were maintained individually and cryopreserved at early passages to safeguard against cross-contamination and ensure identity. No in-house authentication assays were carried out after purchase.
Mycoplasma contamination	The cells were tested for mycoplasma contamination.
Commonly misidentified lines (See ICLAC register)	No commonly misidentified cell lines were used.

Animals and other research organisms

Policy information about studies involving animals; ARRIVE guidelines recommended for reporting animal research, and Sex and Gender in Research

Laboratory animals	The study used 6-9 week old mice. Strains were: C57BL/6J, B6 Albino, BALB/cJ and Ai14 from Jackson Labs.
Wild animals	No wild animals were used in this study
Reporting on sex	Mouse experiments used female mice.
Field-collected samples	No field collected samples were used in the study
Ethics oversight	All the procedures were performed under an animal protocol approved by the MGH and MIT Commitee on Animal Care

Note that full information on the approval of the study protocol must also be provided in the manuscript.

Plants

Seed stocks	N/A
Novel plant genotypes	N/A
Authentication	N/A

Flow Cytometry

Plots

Confirm that:

☒ The axis labels state the marker and fluorochrome used (e.g. CD4-FITC).

☒ The axis scales are clearly visible. Include numbers along axes only for bottom left plot of group (a 'group' is an analysis of identical markers).

☒ All plots are contour plots with outliers or pseudocolor plots.

☒ A numerical value for number of cells or percentage (with statistics) is provided.

Methodology

Sample preparation	Mice spleen, draining lymph nodes, liver and tumor were dissociated into single cells for flow cytometry analysis.
Instrument	Attune NxT Flow Cytometer (Invitrogen). FACS Symphony A3 flow cytometer (BD Biosciences)
Software	Data was analyzed using FlowJo V10
Cell population abundance	N/A
Gating strategy	All gating strategies included doublet cell exclusion gates (FSC-A/SSC-A and SSC-A/SSC-H) and a dead cell exclusion gate (eFluor 506 low or negative with Fixable viability dye). The cell populations within the gate were further analyzed based on expression of markers. Single positive staining and FMO (fluorescence minus one) were used to determine the positively stained cells. The cell populations above the range of 10^3-10^4 on the logarithmic scale was considered as positively stained cells.

☒ Tick this box to confirm that a figure exemplifying the gating strategy is provided in the Supplementary Information.